

Porous Silicon Surface Passivation and Optical Properties

by

Wai-Kit Chang

B.Eng. Materials Science and Engineering
McMaster University, 1993.

Submitted to the Department of Materials Science and Engineering
in Partial Fulfillment of the Requirements for the Degree of

Master of Science
in Materials Science and Engineering
at the

Massachusetts Institute and Technology
June 1996

The author hereby grants to MIT
permission to reproduce and to
circulate publicly papers and
electronic copies of this thesis
document in whole or in part.

Signature of the Author
Department of Materials Science and Engineering
May 10, 1996

Certified by
Professor Karen K. Gleason
Associate Professor of Chemical Engineering
Thesis Supervisor

Certified by
Professor Harry L. Tuller
Professor of Ceramics and Electronic Materials

Accepted by
Professor Michael F. Rubner
Chair, Departmental Committee on Graduate Students

MASSACHUSETTS INSTITUTE
OF TECHNOLOGY

JUN 24 1996

LIBRARIES

Science

Porous Silicon Surface Passivation and Optical Properties

by

Wai-Kit Chang

Submitted to the Department of Materials Science and Engineering
in Partial Fulfillment of the Requirements for the Degree of
Master of Science in Materials Science and Engineering

Abstract

Chemical passivation of porous silicon (PS) surface was studied for the first time by ^1H , ^{19}F , and ^{29}Si NMR, which provide a quantitative and non-destructive investigation of the material. PS was prepared by electrochemically etching single crystal silicon in hydrofluoric acid (HF). Experimental correlations were observed between photoluminescence intensities, mechanical stability, pore structure and the processing of PS.

In freshly made PS, nearly monolayer hydrogen passivation ($10^{15}/\text{cm}^2$) was measured by ^1H NMR and no fluorine was detected by ^{19}F NMR. The hydrogen content was found to increase with exposure to room temperature air, probably a result of water and/or hydrocarbon absorption. The abundance of protons on the PS surface allowed the measurement of ^{29}Si NMR by using the cross polarization (CP) method. Magic angle spinning (MAS), inverse polarization, in addition to sample oxidation and reduction, facilitated the analysis of the spectra, which are compared with FTIR results. The pore surface of the reduced PS was mainly composed of Si-H and Si-H₂ species (chemical shift ~ -100 ppm). After oxidation, the pore surface was mostly covered by Si-H species with either two or three backbonded oxygen atoms (~ -50 and ~ -84 ppm respectively).

Three samples with different thickness (55, 70 and 110 μm) were made by varying only the anodization time (45, 60 and 90 minutes). While ^{29}Si NMR and FTIR indicated similarity in their surface chemistry, photoluminescence measurements (PL) and morphology studies (physical adsorption and desorption) showed significant changes in both surface area and pore diameter with the anodization time. Quantum confinement and chemical passivation theories were considered to explain the correlations between the pore structure and the photoluminescence properties.

Thesis Supervisor: Dr. Karen K. Gleason
Title: Associate Professor of Chemical Engineering

Table of Content

Abstract	2
Table of Content	3
List of Figures	5
List of Tables	7
Acknowledgment	8
Chapter 1. Introduction	9
1.1 History	9
1.2 Formation of PS	10
1.3 Proposed theories of PS	12
1.4 Characterizations of PS	14
1.5 Objectives of this thesis	15
Chapter 2. Experiments (Cell Setup & Operations)	18
2.1 Procedure of PS formation	18
2.2 Preparation of the wafer before anodization	18
2.3 Setup of the electrochemical cell	18
2.4 Collection of PS	19
2.5 Safety Considerations	20
Chapter 3. Processing Experiments and Results	23
3.1 Introduction	23
3.2 Experimental Characterization methods of PS	23
3.2.1 Photoluminescence	23
3.2.2 Thickness	23
3.2.3 Morphology of PS	24
3.3 Electrochemical Etching	24

3.4 Results and Discussion	26
3.4.1 Classification of the processed PS	26
3.4.2 Experimental Results and Discussions	26
3.4.3 Discussion of pore morphology	29
3.5 Conclusion	32
Chapter 4. ¹H NMR and ¹⁹F NMR of PS	43
4.1 Introduction	43
4.2 Introduction to NMR (Nuclear Magnetic Resonance)	43
4.3 ¹H NMR	45
4.3.1 Experiments	45
4.3.2 Results and Discussion	45
4.4 ¹⁹F NMR	48
4.5 Conclusion	48
Chapter 5. Selective PS sample and their characterizations	54
5.1 Introduction	54
5.2 Photoluminescence Characterization Results	56
5.3 FTIR Characterization Results	56
5.4 ²⁹Si NMR Characterization Results	58
5.5 Morphology Results	63
5.6 Conclusion	67
Chapter 6. Conclusions	80
6.1 Summary	80
6.2 Suggested Future Work	82
Bibliography	84

List of Figures

Figure 1.1	Anodic conditions for porous silicon formation and electropolishing in dilute HF aqueous solutions.	17
Figure 2.1	Schematic procedure for processing porous silicon (PS)	21
Figure 2.2	Schematic configuration of the electrochemical cell for PS processing	22
Figure 3.1	Pores on PS surface examined by FEG-SEM (* 200,000)	35
Figure 3.2	FEG-SEM picture of another PS sample covered by graphite (* 250,000)	36
Figure 3.3	Picture of a type A sample (with disintegration on the surface)	37
Figure 3.4	Map for different types of PS in experiment set #1 separated by a dotted boundary, using 1-10 Ωcm Si wafers. D: Disintegrated samples; Numbers: thickness of the PS layer in μm ; A, B, and C in the boxes: types of the resulting PS;	38
Figure 3.5	Map for different types of PS in experiment set #2 separated by a dotted boundary, using 0.01 Ωcm Si wafers. D: Disintegrated samples; Numbers: thickness of the PS layer in μm ; A, B, and C in the boxes: types of the resulting PS;	39
Figure 3.6	Map for different types of PS in experiment set #3 separated by a dotted boundary, using 1-10 Ωcm Si wafers. D: Disintegrated samples; Numbers: thickness of the PS layer in μm ; A, B, and C in the boxes: types of the resulting PS;	40
Figure 3.7	Redrawn of the transition boundaries in set #2 and set #3 as shown in figure 3.5 and 3.6	41
Figure 3.8	Plot of the results in table 3.4. Numbers: % porosity of PS	42
Figure 4.1	Schematic of NMR detection. a) Change of magnetization with time. b) free inductive decay and its fourier transform	50
Figure 4.2	PL spectra of the freshly made PS samples from Spire Corporation. a) 100 mA; b) 50 mA; c) 25 mA;	51
Figure 4.3	^1H NMR spectra of the same three samples after normalization (fresh)	52
Figure 4.4	^1H NMR spectra of the three samples after normalization (2 months later)	53
Figure 5.1	PL results of 3 samples anodized for different times: a) 45 min b) 60 min c) 90 min. Current density: 20 mA/cm^2 , HF conc: 30 wt%	69
Figure 5.2	FTIR Spectra of 3 samples anodized for different times: a) 45 min b) 60 min c) 90 min. Current density: 20 mA/cm^2 , HF conc: 30 wt%	70
Figure 5.3	FTIR Spectra of the 90 minutes sample a) before and b) after annealing at $\sim 200^\circ\text{C}$	71
Figure 5.4	^{29}Si NMR (CPMAS) results for 3 samples with different anodization time: a) 45 min b) 60 min c) 90 min. Current density: 20 mA/cm^2 ; HF	

	conc: 30 wt%; contact time: 3 ms; 1696, 512, 1000 signal averages respectively.	72
Figure 5.5	²⁹ Si NMR result of pure Si (20 signal averages)	73
Figure 5.6	²⁹ Si NMR of two oxidized PS in air at ~ 200°C: a) ~ 4 hours; b) ~ 60 hours;	74
Figure 5.7	FTIR of two oxidized PS in air at ~ 200°C: a) ~ 4 hours; b) ~ 60 hours;	75
Figure 5.8	For the 90 minutes PS sample reduced in HF: a) ²⁹ Si NMR, and b) FTIR;	76
Figure 5.9	²⁹ Si NMR Polarization inversion spectra with different inversion time: i) 0.5 μs; ii) 160 μs; iii) 240 μs; iv) 300 μs; v) 360 μs; vi) 480 μs; vii) 640 μs; viii) 960 μs;	77
Figure 5.10	Pore size distribution: a) sample 1 (45 minutes); b) sample 2 (60 minutes); c) sample 3 (90 minutes);	78
Figure 5.11	Comparison between the 45 and the 60 minutes samples: FTIR NMR and PL	79

List of Tables

Table 3.1	Parameters for three sets of experiments	25
Table 3.2	Classification of the type of resulting PS	26
Table 3.3	Etching rates of selective samples in experiment set #1 and set #2	28
Table 3.4	Density/porosity of the PS samples and the average number of electrons to remove one Si atom.	31
Table 4.1	Summary of the Spire PS samples	46
Table 5.1	Thickness and the anodization time of the final set of samples	54
Table 5.2	Thiele Modulus of the three PS samples	56
Table 5.3	Assignments of the FTIR peaks in the PS samples	57
Table 5.4	Morphologies of PS measured by physical adsorption and desorption	64
Table 5.5	Estimation of the inter-pore wall thickness of the three PS samples	66

Acknowledgment

Well, finally it's my turn! It's really a strange feeling when I am moving the fingers on the keyboard at this moment... I do really owe many (many, many, many...) thanks to a lot of people for all they had done for me. First, I would like to thank my thesis supervisor Karen Gleason for all her patience (though sometimes I don't feel I deserve that) and guidance. Also, I am grateful to Mike Kwan, who had helped me a lot in almost everything (too many to mention here). I also want to thank Leslie Loo for his friendship and all kinds of help (and the invitations for the badminton games too). For Ming Liao...I guess without him, I won't be able to write this acknowledgment now, thanks Ming! (also for all the food you/your wife made) I also want to thank Ken Lau for his friendship and his help during the time we were together (though not too long). I am also grateful to Scott Limb and Catherine Labelle for all their support during these past times.

Besides people in my group, there are some other people I owe my thanks to: Professor Kirk Kolenbrander and his group for their help in my research, Professor Harry Tuller for his advice in this thesis write up, and Professor Anne Mayes, for teaching me so much during the time I was one of her TAs. Also, Dr. Feredoon Namavar (Spire Cooperation) for letting me use his experimental set up, and AnnMarie Cremins for helping me make my first PS samples. For my neighbors in the office, first I want to thank Ginger Tse. I always appreciate the sweets thrown at me every time after TG (they taste good); and all the smiles which make life much more livelier in the office; also Denial, for his friendship; and Lei Zhang, for all her help in the FTIR. Among my course 3 classmates, I want to thank Jung Yoon, Sang Ahn, and Thomas Chen, who have been my good friends for all these three years; and Kamela Crawley, who has been the listener of all my complaints and nonsense.

I would also like to take the chance to mention some of my friends in Hong Kong as well. Though they are not physically besides me, I always feel their presence: Wong Siu To, Eric Lam, Denny Tang, Julian Chu, Christopher Leung, Ming Wong, Josephine Cheung, Elaine Chan, and Chan Man Chong.

Of course, I owe my greatest thanks to my family, who always take me as what I am and offer their help unconditionally whenever I need that.

Before I stop, I want to say thanks to a few more people. First, to Sarah Stock. As being one of the best TAs I've ever met, she has really made the last course I take at MIT enjoyable. Also, to Susan Anderson, for letting me use her cassette player in the studio (actually with many other kinds of help as well) and finally, to Zrinka Orr. Her advice, comments, and encouragement have benefited me a lot (in all aspects). Her friendship during the last few months of my life at MIT really makes the tough time much easier; and I will always remember her guidance in helping me to take the first step into the world which I had never dreamed of before.

Chapter 1. Introduction

1.1 History

Porous silicon (PS) was first discovered in 1956 by A. Uhlir while he was performing electropolishing experiments on silicon [1]. Similar to electropolishing, PS is formed by anodizing single crystalline silicon in hydrofluoric acid (HF). However, lower electrical potentials were applied, yielding a “dark” layer of controllable thickness on the silicon surface. X-ray diffraction showed that this layer was predominately crystalline silicon in the same orientation as the original wafer, but in a porous form. Hence, it possessed a much smaller density and a much higher internal surface area than bulk silicon.

Since then, research on PS has continued to study its properties and its potential applications. In the last decade, most efforts were directed towards PS’s applications in the silicon on insulator (SOI) technologies for two obvious reasons. First, because the original crystal orientation is still preserved after anodization, epitaxial films on PS would have minimal lattice mismatch. Second, the large internal surface area of PS produces rapid oxidization, selectively forming SiO_2 under the single crystal silicon layer.

Pore formation in p-type silicon is generally faster than that in n-type [2]. As a result, by controlling the spatial dopant concentrations in the original single crystalline silicon, the geometry of the PS layer can be modified. This property of PS is being utilized in micromachining to produce a sacrificial layer [3]. For example, PS can be made with adjustable depth at a selective area on the silicon substrate. A sensor bridge is then grown across it, which is followed by etching away of the PS layer, forming a trough below the bridge.

In 1990, another property of PS was discovered by Canham [4]. He showed that photoluminescence (PL) could be achieved at room temperature. Blue or ultraviolet light excitation produced red / orange light emission, which could be seen by the naked eye. Electroluminescence (EL) had also been observed in PS [5, 6]. In contrast, single crystalline Si has an indirect band gap of ~ 1.1 eV at room temperature. Thus, it has only a poor PL efficiency in the infrared range, preventing practical optoelectronic applications. However, the discovery of PS renewed interest in this field, which benefits from the relatively mature and reliable Si based processing technologies.

Several problems still exist in PS. First, its PL efficiency varies with exposure to air [7, 8]. Experiments show that freshly made PS surface is mostly covered by Si-H_x (x = 1,2,3) bonds [9]. When exposed to air, its oxygen content and the number of dangling bonds increase. As dangling bonds are believed to be efficient non-radiative recombination centers for the electron-hole pairs [10], their presence could account for the quenching of PL in air. Besides that, in order to produce efficient devices, good contact with the conducting material is required. Because of its porous nature, metal contacts formed by vapor deposition methods only cover the tips of the pores, although recently there are reports showing efficient filling of the pores by performing metal deposition from the liquid phase [11]. Furthermore, the formation and PL mechanisms of PS are still not well understood. Many seemingly contradictory experimental results have been reported, and numerous theoretical explanations have been proposed, but no one theory has provided a definite, satisfactory explanation for all the observed phenomena. Also, many of these properties are sensitive to the processing methods and the post processing environments. Consequently, one needs careful sample preparation to achieve interpretable experimental results.

1.2 Formation of PS

The most common way to make PS is to anodize it in HF [2]. Other methods were developed recently. That include purely chemical stain etched PS [12], spark erosion PS [13], and PS made from chemical vapor deposition on silica aerosol [14]. But these methods do not show an immediate advantage over the conventional HF anodization method. Therefore, anodization will be used in this thesis.

According to the early studies of semiconductor electrochemistry, the semiconductor - electrolyte interface could be described as a Schottky diode, with the depletion region in the semiconductor side of the interface [2, 15]. The depletion region can affect PS formation in two ways. First, the potential barrier developed there can affect the flow of holes during the reaction. Also, its width will set up a lower limit for the distance between the pores in PS. These features are mainly determined by the potential difference between the Si wafer and the electrolyte, which in turn can be affected by the Si resistivity, HF concentration and the current density.

There are several adjustable parameters in this anodization processing [2, 16]. The first one is the Si doping, which can be altered either in its type (p or n) and in its concentration. Experiments have shown that under similar conditions, p-type Si is etched much faster than n-type Si. This can be explained by the argument that the dissolution of Si involves holes being injected from the valence band to the electrolyte, and is supported by the fact that n-type Si can be etched faster under ultraviolet illumination, which creates excess electron-hole pairs. Using typical current densities ($10 \sim 100 \text{ mA} / \text{cm}^2$), PS with tens of micrometers in thickness can form within 10 to 30 minutes.

Besides the etching rate, the morphology of p-type PS can also be greatly different from that of n-type PS. Generally speaking, under similar conditions, pores from p-type Si are much smaller than that in n-type (nm vs. μm range). Furthermore, in n-type Si, a main pore penetrating from the electrode-electrolyte interface can be easily distinguished from its branches, which grow perpendicular from the main pore and have smaller diameters. On the other hand, in p-type Si, the “main pore” diameters are not much greater than the branches extending from it. Also, these pores are more tortuous and have a wider distribution of orientations than their n-type counter parts.

Also, one can alter the illumination during the anodization process. This influence is greater in n-type Si than in p-type. There is report showing a PL dependence of n-type PS on the illumination wavelength during its anodization process [17]. Also, there is report that employs a periodic illumination scheme to create PS [18].

Another adjustable parameter is the HF concentration, C_{HF} . Usually the electrolyte is made up of HF, H_2O and ethanol. Ethanol is used to improve the wetting properties of the electrolyte. It was found that for both n and p type Si, the pore diameters and the number of branches decrease with the concentration of HF. However, as C_{HF} increases, the inter-pore distance of n-type decreases, while it increases in p-type substrate. Also, a higher C_{HF} indicates a higher conductivity in the electrolyte, which can be reflected by a decrease of the applied potential during anodization under the same processing conditions. (e.g. wafer resistivity, current density)

The current density being used to process PS is another factor that can be used to control its morphology. Generally speaking, the higher the current, the higher the porosity, which can be also be interpreted as a result of the increase in the pores diameters. Furthermore, a higher current density leads to a higher applied potential, if the potential is

too high, electropolishing, instead of the PS formation, occurs, which is also favored by a lower HF concentration (figure 1.1).

Another factor that determines the property of PS is the total anodization time. It has been found that the pore diameters change in the vertical direction perpendicular to the PS surface. The maximum diameter is found in the area closest to the surface. Therefore, it has been proposed that, besides dissolution by electrochemical means at the tip of the pores, the sides of the pores can also dissolve in HF through a chemical means. Since the walls close to the surface are subject to HF for the longest time, the layer dissolved is also largest there.

1.3 Proposed theories of PS

Currently there are three classes of models. One type is based on quantum confinement in the remaining Si “wires”, first proposed by Canham [4]. The reduced dimensions of these wires relax the momentum selection rule, as well as widen its band gap at room temperature. Both of these give rise to the higher visible PL efficiency. The quantum confinement model predicts a blue shift of the PL spectra with a decrease of the wire size. This was observed in thermally oxidized PS in either air or oxygen. During oxidation, SiO₂ forms on the surface of the pores at the expense of the Si atoms in the wires. The blue-shifted PL is usually much weaker than before and has a short, exponential relaxation lifetime (ps ~ ns range), measured by time-resolved PL [19, 20]. However, a red-shifted, non-exponential PL is frequently observed as well with a much longer relaxation time (μs). This could not be explained solely by the quantum confinement model. A branch of this model, which shares the basic idea of the PL mechanism, proposes that instead of wires, quantum dots (nanocrystals) are produced under oxidation [21] when Si at the thinner parts of the undulating wires are totally transformed to SiO₂.

Another type of model [22] suggests that PL originates from the chemical species on the surface of the pores, such as siloxane (SiR₂O)_n and siloxene (Si₆H₆O₃)_n, by comparing the Fourier transform infrared (FTIR) spectrum of PS with these two chemical species, and finding striking similarities between them. However, this cannot be the sole mechanism for PL, as high temperature experiments (~ 1000°C) show that PL is still observable in PS even when these surface chemical species should have all decomposed [23].

The third model, proposed by Koch [24] which is gaining more acceptance, agrees that quantum confinement relaxes the momentum selection rule and widens the band gap. But in addition, there are traps created on the surface of the nanocrystals due to perturbations from oxygen, hydrogen atoms, and the dangling bonds. These traps form a continuous range of surface states inside the band gap. Once the e-h pairs are formed in the nanocrystals, some recombine directly, emitting blue light and contribute to the exponential decay of the spectrum. Alternatively, e-h pairs can diffuse to the surface and recombine through those surface states; or even, they can tunnel through the oxide (which also has a distribution in thickness) to other nanocrystals and recombine there. The latter two mechanisms correspond to the red shifted emission, and the non-exponential decay of PL. This model is more flexible and thus accounts for the different experimental aspects of the PL spectrum.

The actual role of oxidation is very complicated. Annealing the samples in air or in oxygen generally induces a blue shift and a drop of the PL intensity [7]. Nevertheless, there are reports showing different results. Rapid thermal oxidation (RTO) [19] shows an intensity increase in the blue region of the PL spectrum, along with a corresponding decrease in the red part [19]. There are several explanations for these phenomena. The most important one is related to the concentration of dangling bonds, which is very sensitive to the oxidation conditions. Also, the change of the size distribution of the nanocrystals needs to be considered: As oxidation proceeds, the smallest nanocrystals will be completely transformed to SiO_2 , while the larger ones will decrease their size. Furthermore, the smaller the nanocrystals, the more important are the effects of the surface states. Therefore, it is difficult to make a precise prediction of the effects of oxidation before all different influences have been weighted.

Besides the conventional thermal oxidation and RTO, different oxidation methods have been attempted with the hope of minimizing the concentration of dangling bonds. These methods include chemically anodizing Si by ethanol or other oxidizing agents like HNO_3 [25], treatment in boiling water [26], and further anodization in an electrolyte with the oxidizing agent [27]. Again, inconsistent results are reported frequently.

Dangling bonds are generally believed to be the non-radiative recombination centers. Further investigation by electron paramagnetic resonance (EPR) reveals that not all the dangling bonds are of the same type. It is reported that under heat treatment at least two kinds of dangling bonds are formed [28, 29], which is confirmed by measuring the EPR signal while rotating the sample in the fixed magnetic field, as dangling bonds reside on a crystalline

surface with specific orientation will lead to anisotropy. Measurements show that one of them is a trigonal P_b center, which has an anisotropic line shape. The other one is disordered and yields an isotropic line shape, which means those dangling bonds are probably from the amorphous region (Si or SiO_2). These centers do not have the same energy levels in the band gap and their effectiveness to be non-radiative centers are different, a case similar to the Si/ SiO_2 surface.

Humidity in air seems to be also a factor in the oxidation process as well. It has been found that, during oxidation, it is not hydrogen that is detached from Si [9]. Instead, it is the Si-Si backbond that is attacked by the oxidizing agent. As a result, different $Si-H_x$ species will have different oxidation rates. It is found that the oxidation of SiH_2 on a single crystal Si (100) surface gradually occurs through the sequence: $Si_2-Si-H_2 \sim SiO-Si-H_2 \sim O_2-Si-H_2 \sim O_3-Si-H \sim SiO_2$. On the other hand, Si-H on single crystal Si (111) tends to form $O_3SiH \sim SiO_2$ directly. Oxidation behavior is also different in the presence of water. The $Si-H_x$ bonds disappear much faster in a humid environment than in pure oxygen. That suggests Si-H bonds are more vulnerable to the attack by H_2O than oxygen.

Another point worth mentioning is that, for the same material, its EL peak has a smaller wavelength than its PL correspondence [30]. It suggests that the luminescence mechanisms for these two processes may be different.

1.4 Characterizations of PS

Since ordinary scanning electron microscopy (SEM) cannot achieve high enough resolution to visualize the nanometer range pores, the most common methods to investigate the morphology of PS are transmission electron microscopy (TEM), cross section TEM (XTEM), and high resolution SEM (HRSEM). These provide visual, intuitive ideas about the sizes and the distribution of the pores. Other less direct methods were also employed to determine the porosity and the pore distribution, like positron annihilation lifetime measurement [31], Raman scattering [32], and etching rate measurement [33].

Several techniques are being used to probe the chemical nature of PS. The most popular one is FTIR, mainly due its ability to differentiate the chemical bonding environments of hydrogen. However, in order to achieve more quantitative results, careful calibration and samples preparation are necessary. Other surface analysis methods include

Auger electron spectroscopy (AES), secondary ion mass spectroscopy (SIMS), elastic recoil spectrometry (ERS), x-ray photoelectron spectroscopy (XPS), near edge x-ray absorption fine structure (NEXAFS) and Raman spectroscopy. However, they are mostly designed for flat crystal surfaces, not for porous materials, which have a more complex geometry. Within these options, AES, XPS, SIMS are coupled with sputtering facilities which enable depth profiling of PS. However, the different sputtering rates of different elements usually require standards for more quantitative interpretation of the data. Although AES and XPS cannot detect hydrogen, they can be used to provide other chemical information. SIMS and ERS can detect hydrogen, but they are relatively harder to operate. For the detection of dangling bonds, the most commonly used method is EPR [34, 35, 36].

Optical characterization and band gap determination were usually performed by PL. Time resolved PL is also used to measure the recombination lifetime of PS. Besides these, excitation spectra are sometimes employed to study the light absorption properties of the material. These measurements can usually operate with a wide range of temperature in order to study the temperature dependence of the corresponding phenomena.

1.5 Objectives of this thesis

Although several characterization techniques have been used to investigate the properties of PS. Very little research has been done by solid state nuclear magnetic resonance (NMR). My main objective of this thesis is to study the processing of PS and to apply NMR on the samples being made. Because of the relative insensitivity of NMR, a large quantity of sample is required. Therefore, an additional criterion for the processing of PS is to make samples that are thick enough, and at the same time, preserve other properties of PS, both optically and mechanically. Previous work had been studied on the relationships between the PS thickness and the porosity with the anodization time [37]. However, the investigation had not been extended to the range of thickness required in our experiments ($> 50 \mu\text{m}$). Furthermore, the work had not associated the results with the pore structure, surface chemistry, and the PL properties. In this thesis, special attention is directed towards its surface local chemical environment. In order to isolate the influence of surface passivation and quantum confinement effect in the studies, a series of samples is processed under an identical conditions with the exception of only one parameter, which is supposed to change either the surface passivation or the pore structure only. Besides NMR, other characterization methods have also been used to study the samples in order to compare the

results or to provide additional information in the surface chemistry (FTIR) and pore structure (electron microscopy, physical adsorption).

Details of the experimental setup will be described in chapter 2. Chapter 3 and chapter 4 are related to the processing of PS. Chapter 4 and chapter 5 discuss the results from different characterization methods, and conclusion will be in chapter 6.

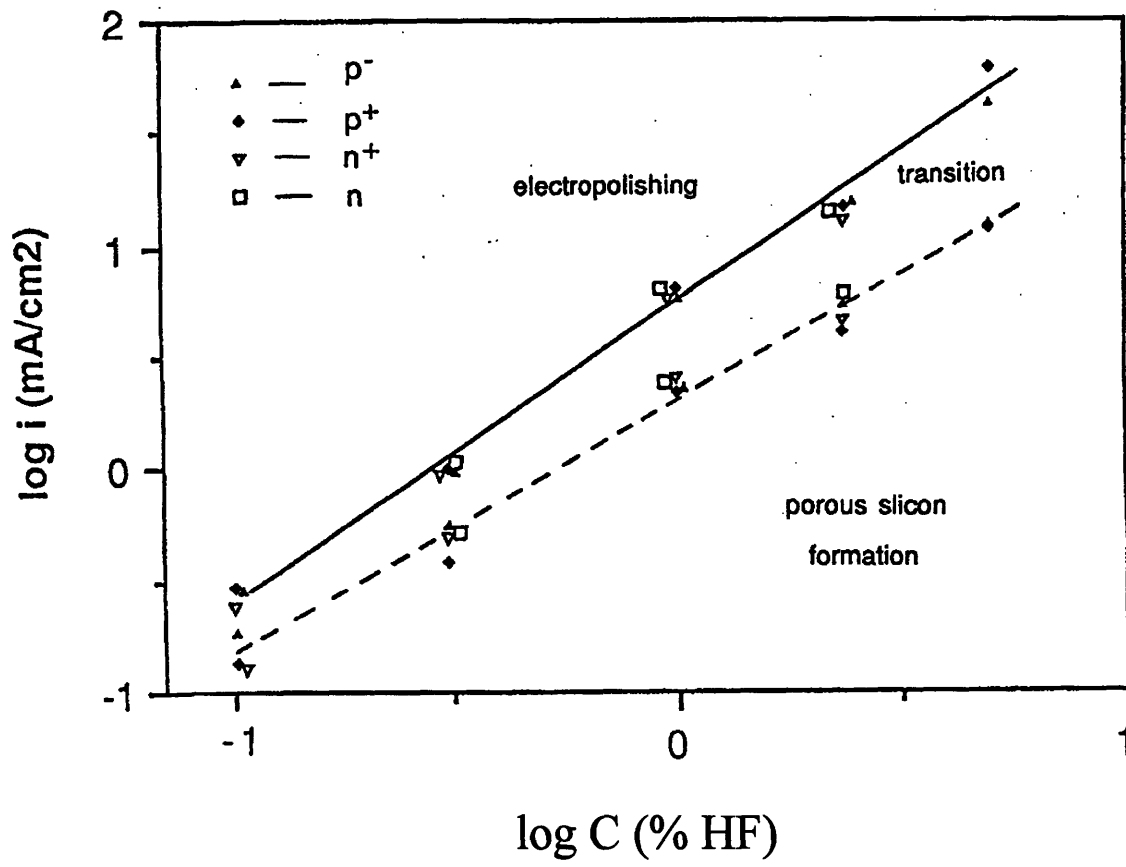


Figure 1.1 Anodic conditions for porous silicon formation and electropolishing in dilute HF aqueous solutions.

Chapter 2. Experiments (Cell Setup & Operations)

2.1 Procedure of PS formation

The steps of PS formation can be briefly described in figure 2.1. First, a layer of aluminum is coated at the back of the silicon wafer, and then it is immediately followed by an nitrogen anneal for 20 minutes. Now the wafer is ready to be anodized in the electrochemical cell with the HF electrolyte. After PS forms on the wafer surface, it can either stay on top of the wafer, or it can be detached from the wafer to form a free standing layer by abruptly increasing the current density in the cell at the end of the experiment. Distilled water is used to wash away HF left on the surface, and then it is blown dry in air.

2.2 Preparation of the wafer before anodization

As mentioned in section 2.1, before the Si wafer is anodized, its back side has to be deposited with an aluminum layer to form an ohmic contact to ensure a good electrical conductivity across the metal-semiconductor junction. This step could be done either in Lincoln lab or in CMSE. Deposition is performed with a thermal evaporator: a tungsten filament is heated up to vaporize the aluminum clips hanging over it in a vacuum (2×10^{-6} torr) chamber, and the resulting aluminum atoms deposit on the wafers underneath. The length of the aluminum clips are chosen in a way such that each of them can contribute to about 700 Å of aluminum in thickness. Deposition is immediately followed by an annealing at 450°C under N₂ atmosphere for 20 minutes to enhance diffusion across the aluminum-silicon interface and form the ohmic contact.

2.3 Setup of the electrochemical cell

The anodization step is the key process in the whole PS formation procedure. Special care had been addressed to ensure its success. Basically there are 3 criteria for the design of the electrochemical cell. First, it has to provide a good electric contact between the positive power supply and the aluminum electrode at the back of the wafer. Second, it has to provide a good seal to protect the same area from the attack of HF. Third, it has to provide an uniform

etching environment for the whole area across the PS surface. In order to achieve these requirements, several measures had been taken.

The configuration of the cell is in figure 2.2. The whole cell is made of Teflon to ensure that it is inert under the attack of HF. For the same reason, viton (a fluorocarbon elastomer) is chosen for the materials of the O-rings. The setup is able to produce PS from either 2" or 4" wafers. An aluminum plate is inserted under the wafer to improve the electrical contact between the wafer and the power supply. An HP E3615A desktop power supply is used to provide a predetermined constant current (0 to 3.24 A) with varying potential (0.5 V to 20 V) during the whole process of PS formation. If a free standing PS is wanted, the high current Soresen DCS 8-125 power supply, which is capable of providing a constant current output up to 125 A (maximum potential output = 8 V), is used to lift the PS layer off from the wafer. In order to support the high current in the detachment process without overheating, a thick wire is required for the current conduction. The cathode of the cell is made of a 5 cm * 5 cm platinum (which is stable in HF) gauze from Fisher Scientific to improve the uniformity of the etching condition across the PS layer. The electrolyte is made by mixing 48 wt% hydrofluoric acid (aqueous) and pure ethanol. The amount of HF used in each experiment is at least about 100 ml to ensure that the concentration is roughly constant during the whole anodization, which is assisted by stirring the electrolyte manually. Also, a fresh electrolyte is mixed for each experiment to improve the reproducibility of the results.

2.4 Collection of PS

For the PS which sits on top of the wafer, the procedure is easier. After the HF electrolyte is removed at the end of the anodization step, the wafer (which is still in the cell) is washed with running distilled water for about 5 minutes until no more visible bubbles (H_2 forms as the product of oxidation of PS by water) form on PS under water. Then the wafer is removed from the cell and blown dried in air.

For the free standing sample, the situation is harder to handle. The pieces which are lifted off from the wafer now float on the water, and hence the remnant HF on their surfaces is hard to washed out. Furthermore, the "still" water environment surrounding these pieces favor the attachments of the bubbles on the surfaces (in the previous case, once the bubbles form, they are driven away by the running water), which will alter the surface chemistry by inhomogenous oxidation. In addition, these floating pieces are hard to collect on the water

surface. In order to lessen these problems, the free standing pieces are collected by filtering them out from the solution. A coarse pore filter paper (and hence fast drainage) with chemical stability under HF is used for this purpose. In this latter case, no specific drying procedure is needed as the PS pieces can dry reasonably fast in the atmosphere.

2.5 Safety Considerations

The most serious part about the safety issue is concern with the usage and disposal of HF. All the experiments were performed in the hood. Also, protective clothings (aprons, face shield, and gloves) were worn all along the process. Used HF was stored in LDPE bottles, which were later collected by the safety office. Also, antidote gel for emergency treatment of HF exposure was ready near the hood, which was kept updated regularly.

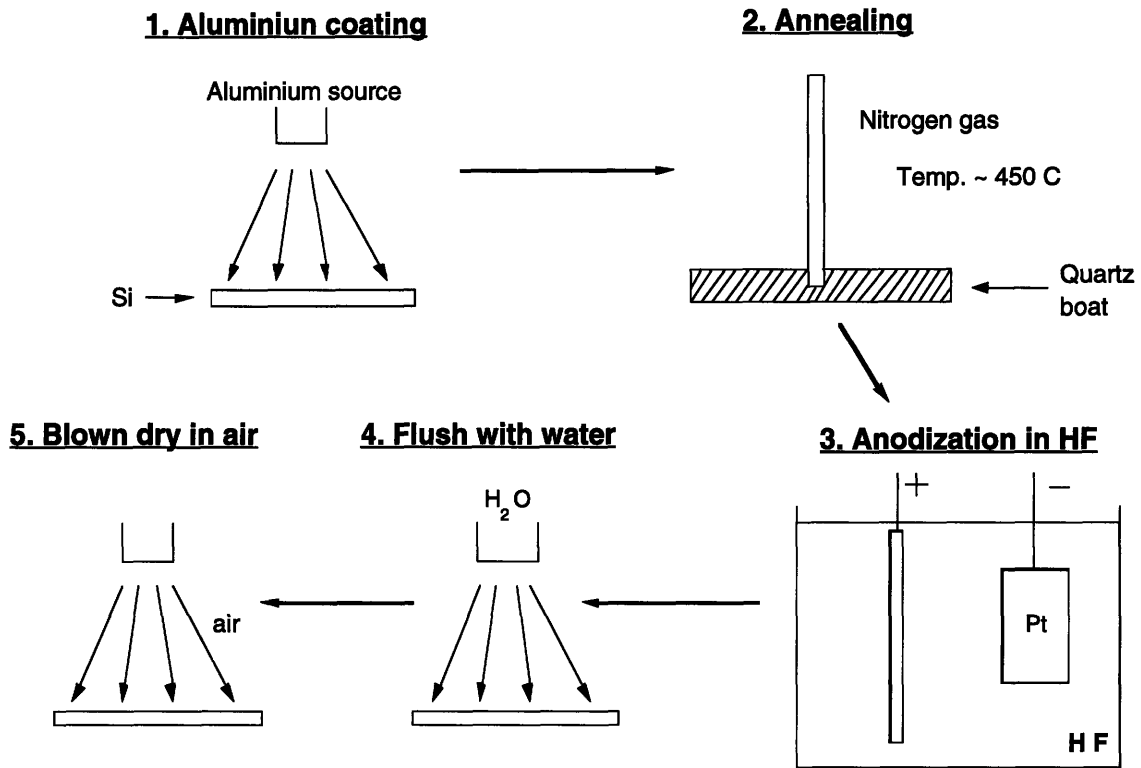


Figure 2.1 Schematic procedure for processing porous silicon (PS)

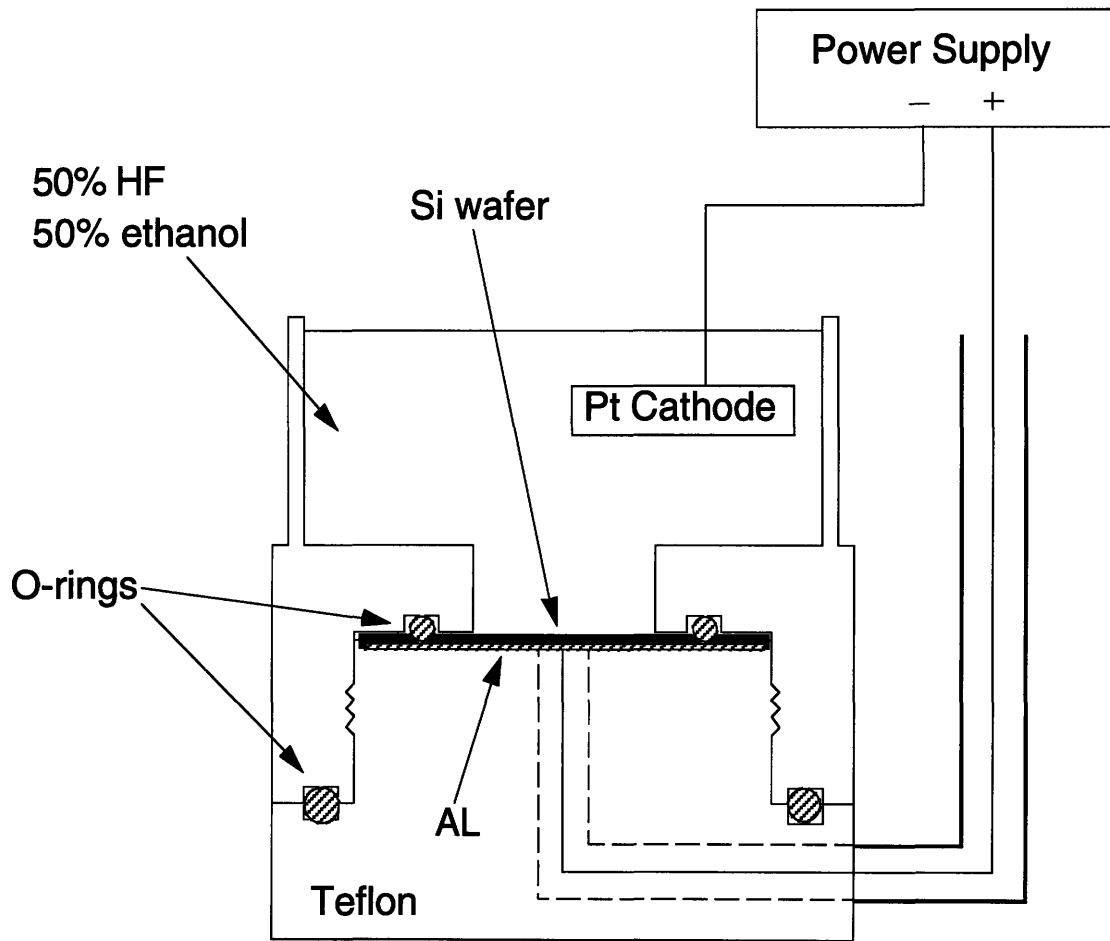


Figure 2.2 Schematic configuration of the electrochemical cell for PS processing

Chapter 3. Processing Experiments and Results

3.1 Introduction

The objective of the first part of the experiments is to search for a suitable range for the processing parameters so that the resulting samples can be compared easily and the results can lead to definite, unambiguous conclusions. This chapter mainly concentrates on the relationships between the physical properties (mechanical strength, morphology and photoluminescence) and the processing conditions of PS. In the second part of the experiment, only one processing parameter is varied, and the corresponding changes in PL, surface chemistry, and other structural features are further investigated.

3.2 Experimental Characterization methods of PS

3.2.1 Photoluminescence

There are two methods for the PL measurements. The first utilizes a 18W handheld UV lamp placed above the sample to excite orange emission from the PS. It provides a first order, convenient and visual, although non-quantitative PL measurement of the material. The second PL measurement was performed in the department of materials science and engineering with the help of Prof. Kolenbrander's group. The wavelength of the excitation laser was 355 nm, and the resulting PL was detected with a Si diode array detector. It provides the quantitative results that can not be achieved by the previous method.

3.2.2 Thickness

A Dektak 8000 profilometer was used to measure the thickness of the PS samples. Due to high porosity, PS is mechanically much weaker than the single-crystalline Si. Small openings (~ 2 mm * 2 mm) were made on the PS surface by scratching it with a razor until the smooth, shiny single crystalline Si underneath was revealed (which had a higher hardness than the razor and hence could not be affected by it). The sample were then put into the profilometer for the thickness measurements, which were done by scanning a height sensitive

stylus across the openings. The drop and rise of the stylus at the walls of the openings were recorded to give the depths of the steps.

3.2.3 Morphology of PS

The morphology of PS was measured by two methods. First, the field emission gun scanning electron microscope (FEG-SEM) was attempted to get a high resolution picture on the surface of the material. A unique feature of the instrument is that it can create an electron beam with a low voltage (compared with the conventional SEM, which used tens of kV). Therefore, it can achieve a higher resolution than the conventional SEM because of its smaller penetration depth in the material. Figure 3.1 shows a magnification of 200,000 fold in one of the PS samples. Some PS samples cause charging under the microscope, and it was suspected that the oxidized surface of PS had become insulating. In that case, a layer of graphite (tens of Ångströms thick) was deposited on the surface of PS. Figure 3.2 shows a picture taken with graphite deposition. Since the pores were so small, the features on figure 3.2 were not very informative because they could have resulted from either the pores or the graphite clusters on the sample's surface.

The second method to measure the morphology of PS was the BET measurement for the surface area and the pore size distribution. Only the three samples made by the final set of parameters were examined by this method. Results will be discussed in more detail in chapter 5.

3.3 Electrochemical Etching

In this part of the experiments, three different sets of experiments had been done. The wafers were p-type, having different doping levels. All three sets of wafers with backside aluminum contacts were supplied from Lincoln Lab. The resistivity of the wafers used in the first set and the third set were in the range of 1 to 10 Ωcm . The resistivity in the second set was 0.01 Ωcm . (Table 3.1) The choice of the resistivities will be justified later.

Set	Resistivity (Ωcm)	Diameter (inch)	Varying Parameter	Constant Parameter
1	1 - 10	2 and 4	t, J	C_{HF}
2	0.01	4	C_{HF} , t	J
3	1 - 10	2 and 4	C_{HF} , t	J

Table 3.1 Parameters of three sets of experiments

In the first set of experiments, HF had a constant concentration (C_{HF}) of 25.5 wt%. The varying parameters were the anodization time (t) and the current density (J). In the second and the third set of experiments, the current density was constant. The varying parameters were the HF concentration and the anodization time. After the anodization step, PS in all three sets of experiments were flushed with distilled water for ~ 5 minutes and blown dried in air before storage at room temperature.

First set:

The electrolyte was prepared by diluting 48 wt% HF aqueous with ethanol. The anodization area of a 2" wafer was ~ 11.6 cm² (3.84 cm diameter). With a current density from 5 mA/cm² to 50 mA/cm², currents of 0.06 A to 0.58 A were used. The anodization area of a 4" wafer was about 55.4 cm² (8.4 cm diameter), and the current used was from 0.23 A to 2.33 A. During the anodization process, bubbles evolved from the etched region. This gas was previously identified as hydrogen [1]. For a typical anodization experiment, the cathode was held about 1.5 to 2 cm above the wafer. After anodization, PS was washed with distilled water. Bubbles (hydrogen) also evolved on the surface on PS during the washing process.

Second Set:

The wafers used in the second set had a resistivity ~ 0.01 Ωcm . The varying parameters were the anodization time and the HF concentration. Current density was kept as a constant at 20 mA/cm². The processing procedures were identical to that in experiment set #1. Only the processing parameters were different.

Third Set:

The wafers had the same resistivities as that in the first set (1 - 10 Ωcm), but the experimental parameters being investigated were similar to those in the second set: the

current density was kept constant (20 mA/cm²), and the variables were the anodization time (t) and the HF concentration (C_{HF}).

3.4 Results and Discussion

3.4.1 Classification of the processed PS

The resulting PS samples could be classified into three different types. The first type of PS (type A) had the strongest PL (orange red) intensity among all when excited by the UV lamp. PL can still be observed even under normal indoor lighting. However, mechanically it is quite fragile. Cracks start to develop on the PS layer surface when it is dried in air during the last processing step. In some extreme cases, there are so many cracks that the whole PS layer just disintegrates into many tiny, curly pieces. (figure 3.3) The second type of PS (type C) is the opposite to this. PS of this type remains firmly intact on the wafer and no visible cracks are found. However, it shows no, or very weak PL, which is hardly observable even in a very dim environment. The third type of PS (type B) is in between these two extreme cases. The PL of it is easily observable in a darkened room, but not under the normal indoor lighting. At the same time, it still remains intact on top of the wafer without forming cracks. Table 3.2 summarize this classification scheme:

Type	A	B	C
PL	Strong	Fair	Weak/None
Mechanical strength	Weak	Fair	Strong

Table 3.2 Classification of the type of resulting PS

3.4.2 Experimental Results and Discussions

First Set:

Generally, porous silicon in this set appeared flat, smooth and uniform on top of the wafer. All of them looked reddish brown. However, a hazy square mark with a slightly different color could be distinguished under close visual examination, which had the same size and shape of the platinum cathode being used in the process. It was found that when the cathode was placed too close to the wafer (< 5 mm), etching of PS would be very

nonuniform. In some extreme cases the etching right under the cathode was so intense that the porous silicon at that area disintegrated locally during anodization. It was also found that while keeping the other parameters constant, using a too high current density, too long an anodization time, or a too low HF concentration would lead to the type A PS: disintegration of porous silicon in the last processing step when it was blown dried in air.

A plot of the PS in set #1 is shown in figure 3.4 with current density (J) versus the anodization time (t). All experiments were performed under a constant HF concentration of 25.5 wt%, and the applied potential fell in the range of 1 ± 0.2 V. Figure 3.4 shows that with this HF concentration and wafer's doping level, both type A and type B PS could be formed. However, type C PS is not found there. It means that all PS in this set were photoluminescent, and this combination of wafer's doping level and HF concentration leads to a relatively weak mechanical strength in PS. Figure 3.4 further shows that there is an upper limit for the combinations of J and time that can be used to process PS which are mechanically acceptable. That is the dotted line in figure 3.4. The numbers beside the PS in figure 3.4 are the thickness of the PS layer in μm . It shows that the PS's thickness increase when the processing parameters chosen are moving towards that limit. However, once that limit is crossed, the mechanical stability of PS is lost. This upper limit, obtained from the figure, is approximately $800 \text{ mA/cm}^2 \cdot \text{min}$. This can be used as a rule of thumb for further experiments under similar conditions.

Several additional characterization methods were employed to examine the PS samples processed in the second part of the experiments, including NMR and BET. Because of their insensitivity, these two methods require a relatively large amount of samples. It had been estimated that in order to get enough sample for NMR, the thickness of the PS has to be at least $40 \mu\text{m}$ for a 4" wafer, or at least $160 \mu\text{m}$ for a 2" wafer. From figure 3.4 it was found that the samples in this set could not meet that requirement. Since too long an anodization time could lead to a disintegration of PS when it was dried in air (type A samples), it was not possible to get a thicker sample by increasing the anodization time. Therefore, the etching rate had to increase. For this reason, wafers with a high doping level, which are known to have a higher etching rate [16] were investigated.

Second Set:

The most obvious observable difference between PS formed in this set and that from the set #1 was that they were not reddish-brown in color. Instead, they appeared greenish-

blue to dark gray. In terms of the surface structure, PS in this set were as smooth and uniform as that in set #1. However, the hazy mark related to the platinum cathode were no longer observable, which was at the same position as before.

Besides, it had been found that, with the same HF concentration and current density in experiment set #1, PS formed in set #2 could be etched for a longer time (> 200 minutes) without disintegration during the last brown drying step. Also, compared with the PS made in the set #1 under a similar anodization situation, PS in this set have a slightly higher etching rate ($\mu\text{m}/\text{min}$). This was shown in table 3.3:

Sample	Experiment set	$J(\text{mA}/\text{cm}^2) / C_{\text{HF}} (\text{wt}\%)$	Etching Rate ($\mu\text{m}/\text{min}$)
30	1	20.6/25.5	0.88
44	2	20/25.5	1.125
39	2	20/25.5	1.29

Table 3.3 Etching rates of selective samples in experiment set #1 and set #2

For example, when $C_{\text{HF}} = 25.5 \text{ wt}\%$, and $J \sim 20 \text{ mA}/\text{cm}^2$, 40 minutes anodization could produce about $35 \mu\text{m}$ of PS in the first set, so the etching rate was about $0.88 \mu\text{m}/\text{min}$. However, in the second set, with the same C_{HF} and J , 140 minutes anodization resulted in about $180 \mu\text{m}$ of PS, so the etching rate was about $1.29 \mu\text{m}/\text{min}$.

The processing results of this set are summarized in figure 3.5, with anodization time (t) verses HF concentration (C_{HF}) as the axes. Similar to figure 3.4, figure 3.5 can be basically divided into two different regions: the type A region in the left of the figure, and the type C region in the right. The dotted line was the ‘boundary’ of these two regions. Type B PS, which is supposed to be in between these two regions, does not appear here. It means PS in this set changes from one type to another abruptly across the boundary. Therefore, in terms of searching for a suitable anodization parameter window, this was not a suitable choice because the region of most interest, B, did not exist in this system. As a result, although PS with higher thickness and mechanical strength was possible in this set, it still could not meet the overall requirements.

Third Set:

Considering the samples in experiment set #1 and #2, wafers with a higher resistivity (1 - 10 Ωcm) were used again. The results of this set were plotted in figure 3.6. Again, several regions corresponding to different types of PS could be identified. The main difference between this figure and figure 3.5 was that the type B PS was found in the system. That meant the change of the resulting PS properties were more gradual in this system. Along the “band” of type B PS, the thickness of the PS layer increases with etching time and HF concentration. This was a valuable feature for deciding a parameter window of PS since “good” PS samples that were both large enough for NMR and BET measurements, as well as having a reasonable mechanical strength could be processed by choosing suitable parameters along this band. The final processing parameters, which were discussed in chapter 5, were chosen by studying this set of experiments as the guideline.

3.4.3 Discussion of pore morphology

Most of our results regarding the effects of doping level and the HF concentration on PS properties were consistent with previous work [16], which can be summarized as followings: for the p-type Si, increases in the current density will lead to : 1) larger pore size, 2) similar inter-pore distance, and 3) higher etching rate ($\mu\text{m}/\text{min}$). An increase in the doping level results in three outcomes: 1) larger pores, 2) larger inter-pore distances, and 3) higher etching rate ($\mu\text{m}/\text{min}$). On the other hand, a decrease in the HF concentration results in: 1) larger pores, 2) smaller inter-pore distance, and 3) slower etching rate ($\mu\text{m}/\text{min}$). The only difference we observed was that an increase in current density seemed to decrease the inter-pore distance.

The most important factor that determines the mechanical stability of PS is the inter-pore distance, or in another words, the diameter of the Si "wires". If it is small enough, then the network of the wires can become mechanically quite flexible. Experiments had been performed to show that the free standing layer of PS acts like a sponge, which can expand and contract repeatedly under the absorption and desorption of ethanol [38]. However, if the wires are too thin, they can be broken easily under external force. That is the case when the type A PS was dried in air after flushing with water at the end of the processing step, where the tensile stress (originated from the capillary force at the gas-liquid interface) created during the process was identified to be the source that destroyed the Si wires [39, 40]. This means that although a high porosity usually means a weaker PS, there is no direct relationship between the two properties. To overcome the problem of the capillary force, PS

had been dried supercritically [39, 40], in that case mechanically stable, high porosity (up to 90 %) PS, with Si crystallites < 30 Å, had been reported.

From the above information, it is not difficult to understand the trend of the PS mechanical strength shown in the previous figures. In figure 3.4, the increase in the current density will decrease the potential barrier at the pore-electrolyte interface, and hence the depletion width, which will indirectly decrease the lower limit for the inter-pore distance. Also, the higher the current density, the higher the applied potential, and the closer to the electropolishing regime of Si. Both of them can lead to an early disintegration of PS compared to the experiments performed at a lower current density. It had been found that the transition from PS formation to electropolishing starts from $\sim 60 \text{ mA/cm}^2$, which is close to our results (figure 3.4). The transition boundary in figure 3.4 can be approximated by an inverse relationship between the current density (J) and the anodization time (t). That is: $J = \text{constant} \cdot t^{-1}$, where the constant in the equation $\sim 800 \text{ mA/cm}^2 \cdot \text{min}$ (determined from the figure). It means that along the transition boundary, the same amount of holes ($J \cdot t$) had been used to produce PS. Since these samples had the same thickness ($\sim 35 \mu\text{m}$), it can be concluded that they had similar porosity. Assuming two holes are used to remove one Si atom, the porosity of the samples along the boundary were estimated to be $\sim 86 \%$.

The decrease of HF concentration leads to a decrease in the inter-pore distance, and therefore forms a 'weaker' PS. The increase of the doping level leads to an increase in the inter-pore distance, and hence an opposite effect was observed. Furthermore, the higher etching rate ($\mu\text{m}/\text{min}$) in the heavily doped PS suggests that branching of the pores is less frequent than that in the lightly doped PS, which also favors the enhancement of the mechanical strength of the material. This can be observed by comparing figures 3.5 and 3.6. Note that the boundaries that separate different types of PS had shifted from the lower concentration to a higher concentration when a lightly doped Si (set #3) was used to make PS. The boundaries had been redrawn in figure 3.7. The transition of the samples in set #3 was taking place about 20 wt% higher than that of set #2. That indicates a higher HF concentration has to be used to balance the effect of the lower doping level in order to maintain the minimum inter-pore distance for mechanical strength. A further observation supports this result is that: in order to measure the thickness of PS by the profilometer, 'openings' were made in PS by scratching the surface with a razor. These 'openings' could be easily made in PS from the first and third set. However, PS from the second set were much harder and the openings were more difficult to create.

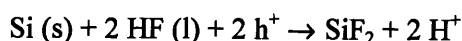
Following this line of reasoning, it means that under a constant anodization condition, the inter-pore distance will decrease with time (as observed from figure 3.5 and 3.6). That can be due to two processes: (a) the branching of the pores with time and (b) the widening of the pores by pure chemical reaction in HF. For the first process, there is a lower limit for the inter-pore distance as the width of the depletion layer around the pores will affect the flow of the current to the pores. However, although the second reaction ($< 1 \text{ \AA}/\text{min}$) is much slower than the first one, it does not have any lower limit. Therefore in theory, as long as there is enough HF available, the widening of the pores will go on with time. Since the diameters of the pores are expected to be in the order of tens of \AA , the relatively change of the pore diameters are not insignificant in the range of the anodization time being used in the experiments (45 - 200 minutes).

For several PS samples, the weights of the wafers before and after anodization were measured. Combining with the thickness of the samples obtained from the profilometer, densities of the samples were calculated. Furthermore, from the anodization current and time, we calculated the number of holes consumed in the process. The results were shown in table 3.4.

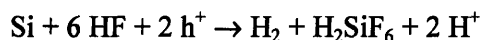
Sample	Set	Time (min)	C_{HF} (wt%)	Density, ρ (g/cm^3)	Porosity ($(1-\rho/\rho_{\text{crystal}})*100\%$)	Ratio (e^- to Si)
41	2	45	20.7	0.69	70	2.20
44	2	200	25.5	1.20	48	2.17
46	2	200	22	0.96	59	1.92
47	2	200	20	1.01	57	2.08
51	3	90	30	0.94	59	1.96
56	3	105	30	0.92	60	1.93
58	3	90	32	1.13	51	2.19
63	3	60	32	1.07	54	2.06

Table 3.4 Density/porosity of the PS samples and the average number of electrons to remove one Si atom.

From previous work, it had been found that two holes are needed in order to remove a Si atom from the bulk. The initial reaction proposed as the initial step was [41]:



In our results, the average ratio of the holes to the Si atoms being consumed was 2.05 ± 0.12 , which is consistent with this previous work. SiF_2 is an intermediate which will further decompose into other products. The actual reaction path is still not certain. Although there are several proposals for the intermediate steps, they all end up in the same end product: H_2SiF_6 , which is soluble in water. The overall reaction was written in this form:



Note that in this overall reaction, 6 HF molecules and 2 holes are needed to remove 1 Si atom from the surface.

The plot of the porosity results is shown in figure 3.8. It was found that the porosity of all the samples were similar. Only sample # 41 had a much higher porosity than others, which may be due to its high current density (60 mA/cm^2) compared with the rest (20 mA/cm^2). The figure did not show an obvious increase in porosity towards the boundary. However, it did show that PS with a higher doping level could achieve the same range of porosity as the weakly doped PS, when they were etched under a lower HF concentration.

3.5 Conclusion

Experiments were done to look for a set of parameter values for making porous silicon. The final goal was to produce a set of PS samples such that they could be compared easily and the results could lead to definite conclusions about the properties of the material.

Briefly the experiments could be divided into three sets, according to the doping level of the original Si wafers and the parameters being examined. Resistivity in set #1 and set #3 were $10 \text{ }\Omega\text{cm}$, while the resistivity of set #2 was $0.01 \text{ }\Omega\text{cm}$. In set #1, the concentration of HF was constant, and the varying parameters were the current density and the anodization time. In set #2 and set #3, current density was kept constant, while the HF concentration and the anodization time were the variables.

It was found that the resulting PS could be approximately classified into three types. Type A PS had the brightest PL than the others, which was observable even under the normal indoor lighting. But at the same time they also had the highest mechanical instability. They could even be destroyed by the capillary force created from the evaporation of water inside

the pores during the drying step in air. At the other extreme, type C PS had no difficulty with mechanical stability. However, its PL was so weak that it could hardly be observed even in a very dark room. The last type of PS, type B, was in between. PS in this type had enough mechanical stability to support itself, and at the same time, its PL was strong enough to be observed under a darkened room.

Most of the influence of the parameters (doping levels, current density, anodization time, and HF concentration) on PS morphology was found to be consistent with previous work. This work supports an hypothesis that connects the anodization conditions, the porous silicon's morphology, their mechanical stability and PL properties. In our hypothesis, the most important parameter that characterizes porous silicon's properties is the inter-pore distance. A small inter-pore distance indicates mechanical instability and, according to the quantum confinement model, a strong PL emission. Therefore, the link will be simplified to the determination of the relationship between different anodization conditions and the inter-pore distance. It was found that, an increase in the current density, and an increase in the anodization time will lead to a smaller inter-pore distance, while an increase in the doping level, and an increase in the HF concentration will achieve the opposite effect.

From experiments, it was found that, for the Si wafers with a higher doping level (i.e. set #2), the change from the stable (mechanically) regime to the unstable regime was very abrupt. The mostly desired regime (B), which contained both PL and mechanical strength, was not found there. On the other hand, the change for Si with a smaller doping levels was more gradual, where a “band” of type B PS was found to be extending towards the direction of increasing anodization time and HF concentration. Furthermore, the thickness of PS was found to increase along the band. This is a valuable feature, as a thick ($> 100 \mu\text{m}$) PS was needed for further characterizations in order to gain more information about the surface chemistry of the material. The need to examine the surface chemistry of PS is increased by the fact that PL intensity of type A PS from set #2 is found to be much lower than that of type B from set #1. This contradicts the pure quantum confinement model as it predicts a similar PL intensity for Si wires with similar dimensions. This discrepancy may be due to other factors like the non-radiative recombination traps, or surface chemistry.

The density and porosity were calculated for several samples. The results showed that porosity itself was not directly related to the mechanical strength of PS, but it did show that PS made from Si with different resistivities could achieve similar porosities by using different HF concentrations. Furthermore, the number of holes consumed in the process was calculated

from the current and anodization time. Compared with the number of Si atoms removed, the average ratio of (holes)/(Si atoms) was determined to be 2.05 ± 0.12 , which was consistent with the previous work. Also, from the overall reaction, it was found that three HF molecules were needed every time a hole was consumed. This information was useful in the calculation of other properties in the experiments, which will be further discussed in chapter 5.

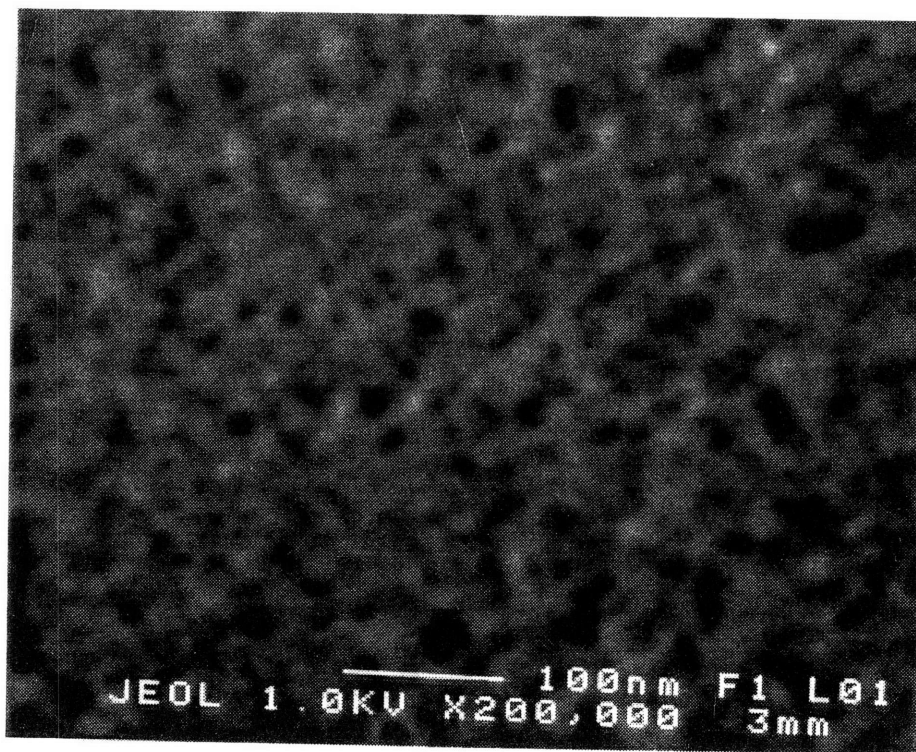


Figure 3.1 Pores on PS surface examined by FEG-SEM (* 200,000)

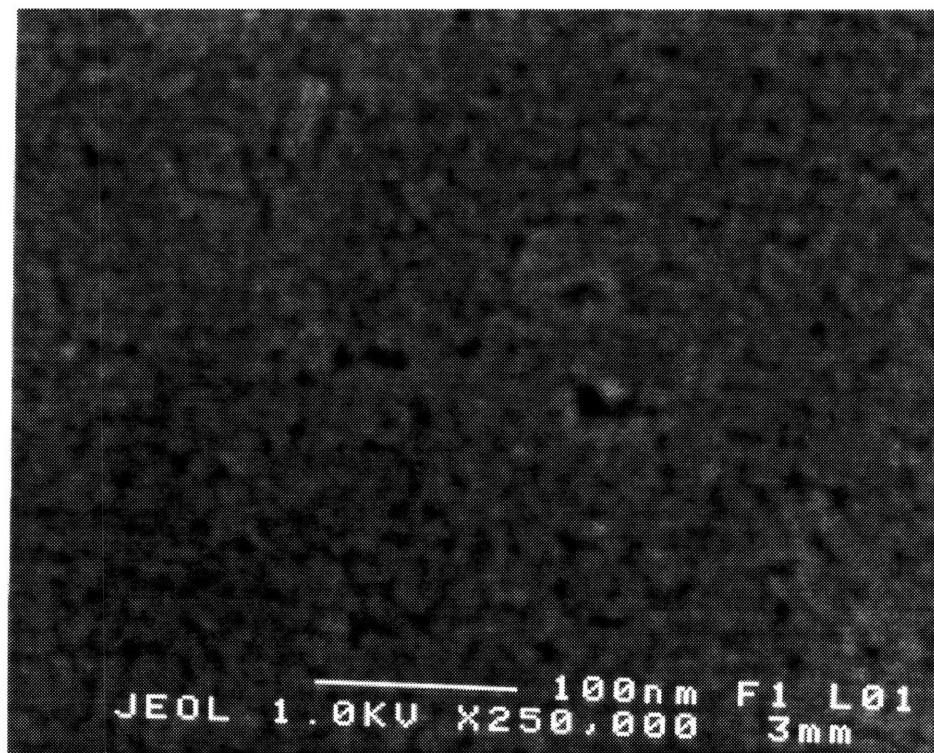


Figure 3.2 FEG-SEM picture of another PS sample covered by graphite (* 250,000)

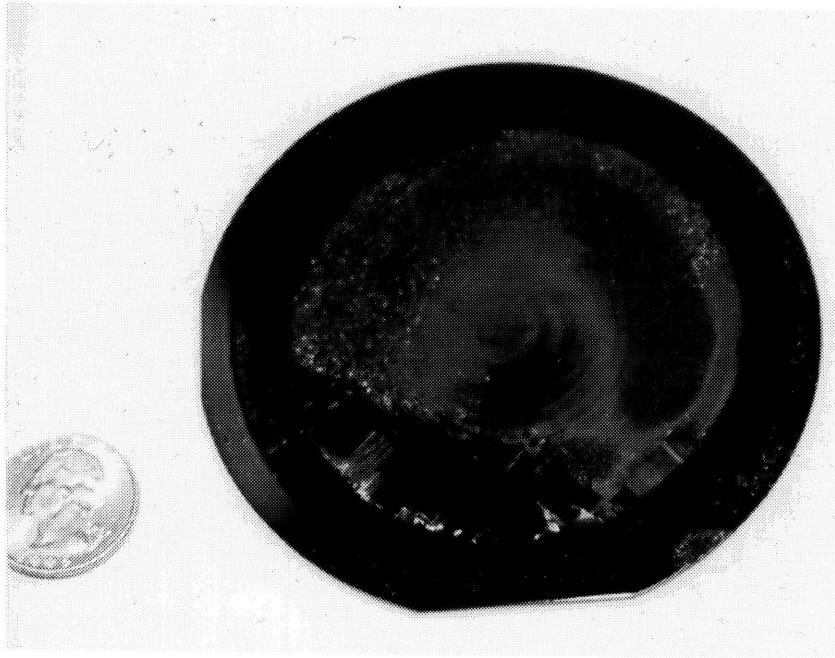


Figure 3.3 Picture of a type A sample (with disintegration on the surface)

Results in experiment set #1

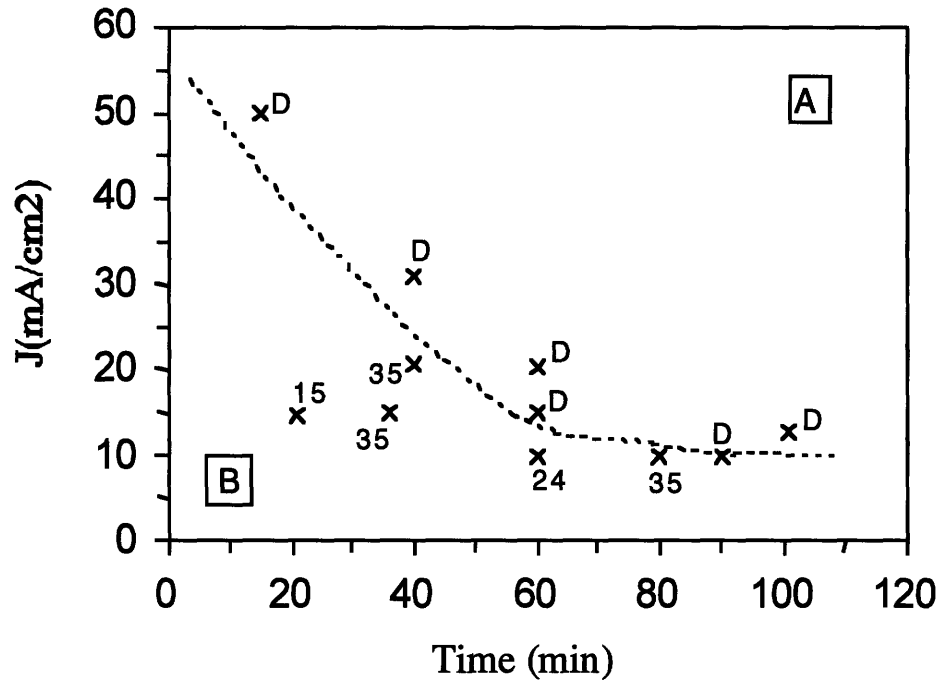


Figure 3.4 Map for different types of PS in experiment set #1 separated by a dotted boundary, using 1-10 Ωcm Si wafers. D: Disintegrated samples; Numbers: thickness of the PS layer in μm ; A, B, and C in the boxes: types of the resulting PS;

Results in Experiment set # 2

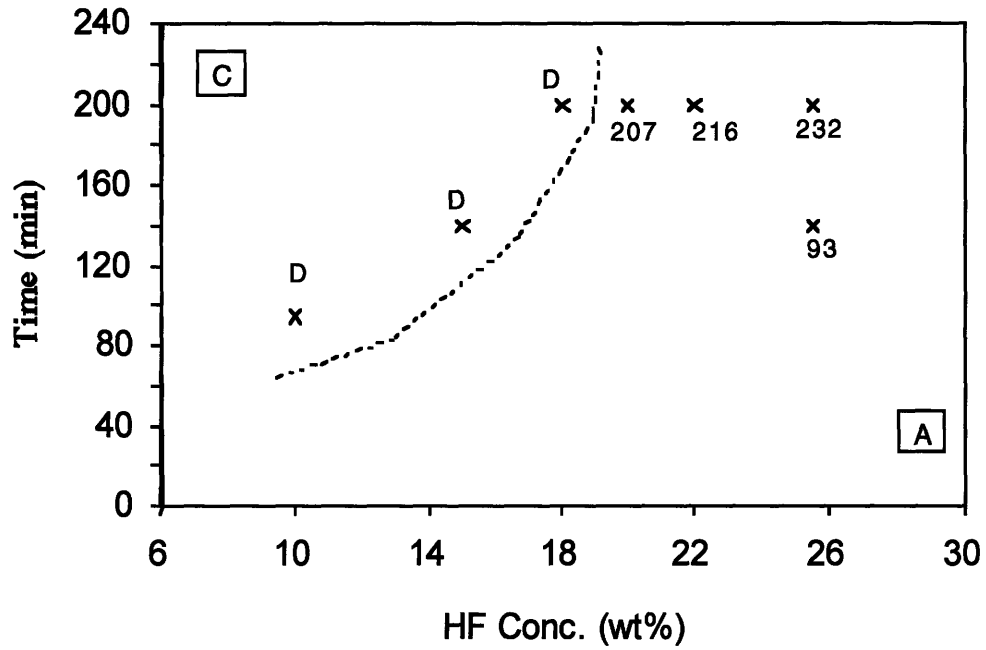


Figure 3.5 Map for different types of PS in experiment set #2 separated by a dotted boundary, using 0.01 Ωcm Si wafers. D: Disintegrated samples; Numbers: thickness of the PS layer in μm ; A, B, and C in the boxes: types of the resulting PS;

Results in Experiment Set # 3

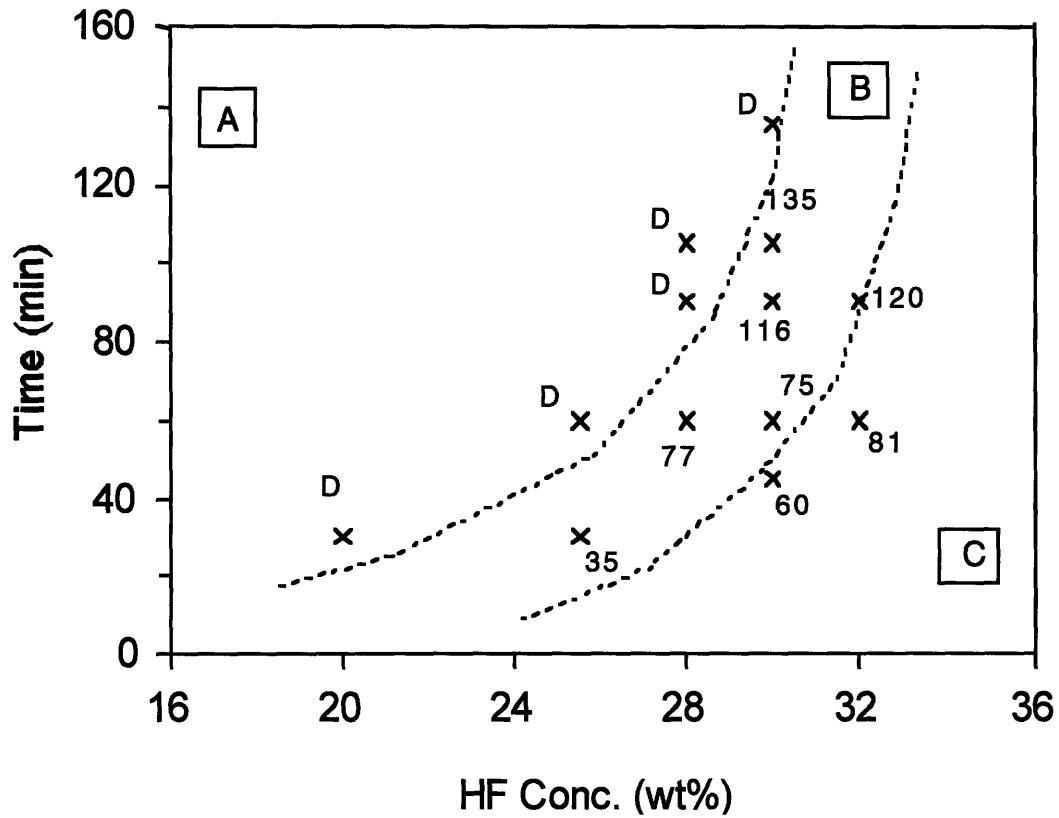


Figure 3.6 Map for different types of PS in experiment set #3 separated by a dotted boundary, using 1-10 Ωcm Si wafers. D: Disintegrated samples; Numbers: thickness of the PS layer in μm ; A, B, and C in the boxes: types of the resulting PS;

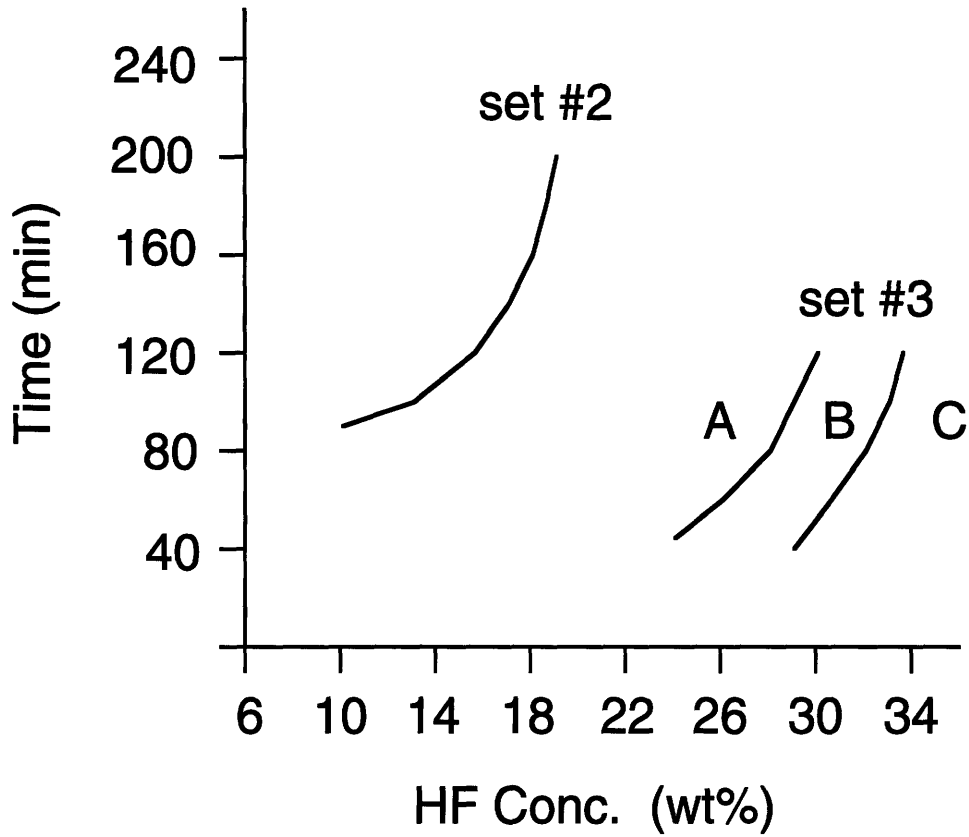


Figure 3.7 Redrawn transition boundaries in set #2 and set #3 as shown in figure 3.5 and 3.6

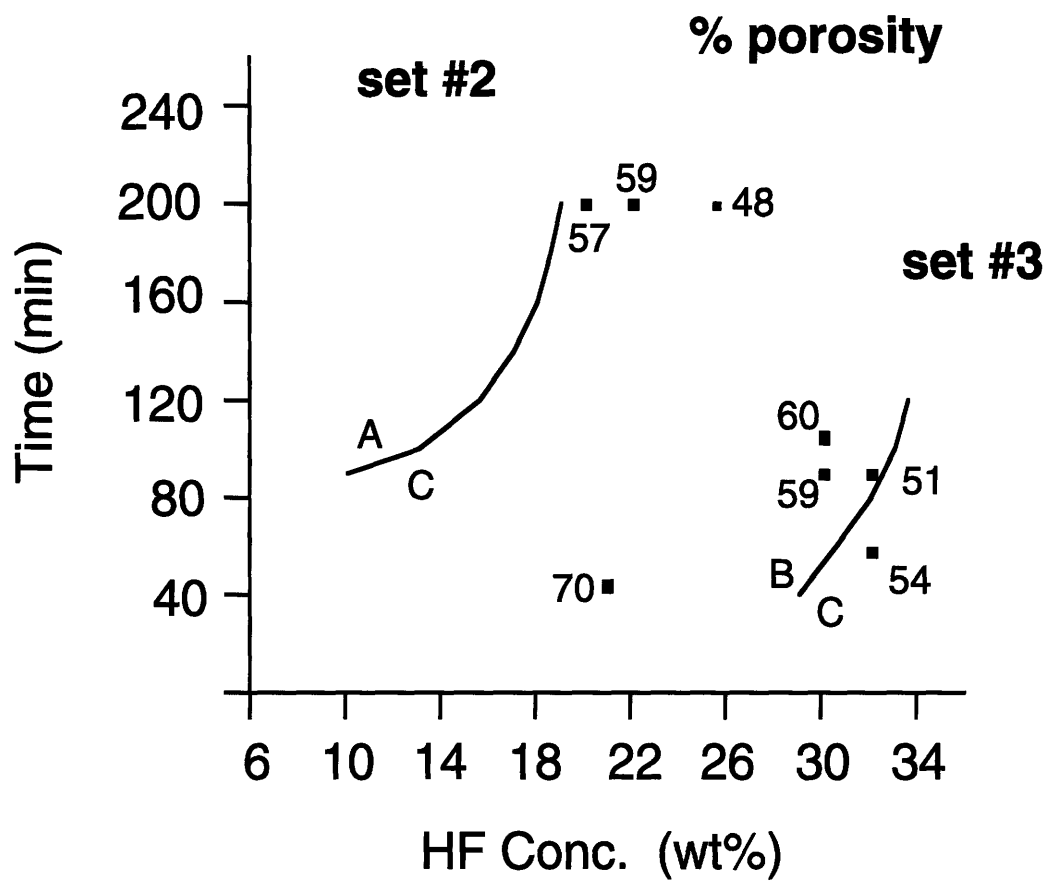


Figure 3.8 Plot of the results in table 3.4. Numbers: % porosity of PS

Chapter 4. ^1H NMR and ^{19}F NMR of PS

4.1 Introduction

As mentioned in the previous chapter, the photoluminescence properties of PS may be related to its surface chemistry, although the role it plays is still uncertain. Therefore it is desirable to get a better idea of the chemical configuration of the PS surface.

Several characterization methods have been used to study PS. However, due to their limitations, they cannot provide a reliable quantitative measurement of the hydrogen content in the material. For a qualitative investigation, FTIR is usually employed because of its ease of use and its ability to detect different hydrogen bonding configurations. However, although there is a general consensus about the assignments for most of the peaks measured in PS, some of them are still ambiguous (which will be discussed in more detail in chapter 5). Besides, FTIR results do not readily give quantitative interpretations without very careful calibration with the standards.

^1H NMR is unique, compared with other methods, because of its ability to provide quantitative results. In the past, the main reason against the use of NMR is its low sensitivity, which means a minimum quantity of sample has to be used in order to ensure a reasonable signal to noise ratio of the NMR spectra within a reasonable measurement time. This may lead to some inconveniences. Besides, the signal in the solid state NMR spectrum is usually so broad that it is hard to extract useful chemical information (chemical shift) from the measurement. Presently, however, both the detection methods and instruments have improved. Furthermore, the large surface area in porous silicon should be able to provide adequate protons for the NMR measurements.

4.2 Introduction to NMR (Nuclear Magnetic Resonance)

NMR exploits the magnetism of certain nuclear isotopes. A nucleus that possesses a magnetic moment μ has an angular momentum $\hbar I$. They are related by the following equation:

$$\mu = \gamma \hbar I \quad (4.1)$$

where γ is the magnetogyric ratio, which is nuclear dependent.

Under an external magnetic field B_0 , the energy level of the nucleus with spin $I = 1/2$ splits into two, with opposite spin directions. The energy between these two levels is:

$$E = \gamma \hbar B_0 \quad (4.2)$$

Therefore the resonance is frequency is:

$$\nu_0 = (\gamma B_0) / (2\pi) \quad (4.3)$$

In equilibrium, there are more spins at the lower energy level with the same direction as B_0 . Therefore the magnetization of the sample, $M_0 = \sum \mu$, is also in the direction of B_0 (defined as the **Z** direction). In a fourier transform NMR experiment (figure 4.1), a pulse (or pulse sequence) at radio frequency (which generates another magnetic field B_1) is used to perturb M_0 from its original direction (usually 90° to the **Y** axis), and the subsequent relaxation of M back to equilibrium is measured as a decay of the magnetization along the **Y** axis with time. (That is called free induction decay). The signal is then fourier transformed to the frequency domain to yield the spectrum.

In a real sample, the local magnetic field at the nucleus is not just B_0 , but also includes the effects from the surrounding magnetic moments and the electronic environment around the nucleus. Therefore, NMR signals can provide structural, as well as chemical information of the sample on a molecular level, like the coordination numbers, local symmetry, and inter-nuclear bond distance.

One of the advantages of NMR is that the sample preparation is very simple. No specific requirements are needed. Also, NMR is inherently quantitative. This means that for a given nucleus the proportionality factor relating the area under a peak to the number of nuclei giving rise to the signal is not at all sample-dependent. Furthermore, different information about the sample can be extracted by using different pulse sequences to perturb M and measure the resulting magnetization. This provides more flexibility in the measurements.

4.3 ^1H NMR

4.3.1 Experiments

In this set of experiments, we were quantifying the amount of proton nuclei (spin) in the samples. Three PS samples used in the experiments were supplied by the Spire Corporation, MA. They were all p-type (100) wafers, with resistivity starting from 1 Ωcm to 10 Ωcm . The electrolyte was made up of 48% aqueous HF and ethanol in a 1:1 ratio. That was equal to 24 wt% of HF. These configurations were the same as set #1 mentioned in the last chapter. The anodization time was 30 minutes. The only difference among them was the current density being used in anodization. The current densities for sample A, B, and C were 100 mA/cm^2 , 50 mA/cm^2 and 25 mA/cm^2 respectively, and their thickness were ~ 2.2 , ~ 4.5 , and ~ 10.7 μm respectively, measured by cross-sectional environmental SEM. Compared with our results of set #1 which were processed under similar conditions, it was found that the Spire samples had a much smaller thickness ($\sim 10 - 20$ %). The reason for this discrepancy is not certain.

^1H NMR experiments were performed with a probe designed for low proton detection [42]. Special steps were taken to minimize the proton signal from the background. Si slivers deposited with poly(methylmethacrylate) (PMMA) of different concentrations were used for the calibration of the instrument. It had been shown that the response of the instrument to ^1H was linear in the range as low as 10^{18} nuclei [42]. However, in our specific case, it was piecewisely linear. The background signal for the probe was also measured and found to be negligible compared with that from the samples. The proton resonance frequency in our experiments was 270 MHz. The 90° pulse time was about 4 μs , and the recycle delay was about 15 s. About 7000 signal averages were employed for each spectrum.

4.3.2 Results and Discussion

Figure 4.1 is the PL measurements for the 3 samples described above about one hour after they were made. It showed that the trend for both the PL intensity and the peak position were not monotonic. Sample B (50 mA/cm^2) had the highest PL intensity among three of them. However, in terms of the peak position, the trend was reversed. Sample B had the lowest wavelength. The FWHM of the samples increased from 110 to 150 nm for sample A to sample C. They all showed a tail in the higher wavelength side.

The NMR signal of the samples after normalization by their volumes are shown in figure 4.2. It shows that the proton concentration decreases with anodization time. This result was quite unexpected. From the last chapter, it could be predicted that the porosity, the pore diameters, and the etching rate ($\mu\text{m}/\text{min}$) of the $100 \text{ mA}/\text{cm}^2$ sample would be higher than that of the $25 \text{ mA}/\text{cm}^2$ sample. Therefore, the surface area, as well as the hydrogen content of the $100 \text{ mA}/\text{cm}^2$ sample should be higher as well, if we assumed the surface chemistry of the samples were similar. Compared with the corresponding PL spectra in figure 4.1, it was found that there was no direct correspondence between the PL results and the ^1H NMR results. From the absolute value of the data, it has been estimated that, by assuming the surface area of PS to be around $400 \text{ m}^2/\text{cm}^3$, the hydrogen concentration on the pore surfaces is on the order of $10^{15} / \text{cm}^2$. As the number of bonds on the Si monolayer are ranging from $7.8 \cdot 10^{14}/\text{cm}^3$ ($\{111\}$ planes) to $1.4 \cdot 10^{15}/\text{cm}^3$ ($\{100\}$ planes) [43]. This provides confidence on our experiment data, and shows that the coverage of our samples are close to a monolayer. The calculated results are summarized in table 4.1

	Sample A (100mA)	Sample B (50 mA)	Sample C (25 mA)
Thickness (μm)	8	3.42	1.68
Volume (cm^3) (10^{-3})	1.56	0.32	0.4
Surface area (cm^2)	6240	1280	4600
^1H Content (10^{18})	2.1	0.45	4.1
^1H concentration ($/\text{cm}^3$) (10^{21})	1.35	1.41	10.25
^1H concentration ($/\text{cm}^2$) (10^{14})	3.38	3.53	25.6

Table 4.1 Summary of the Spire PS samples

Figure 4.2 shows a larger difference between the 100 mA and the 50 mA sample than that in table 4.1. This is probably due to the piecewisely linear calibration curve. The three ^1H NMR peaks are roughly at the same positions. However, since the range of chemical shift for ^1H is so small (~ 10 ppm) that any existing individual peaks cannot be resolved in the spectra, and hence no conclusions about the surface chemistry can be drawn. That is the reason to apply ^{29}Si NMR in the next chapter, which has a much larger range of chemical shift. However, certain observations can still be made from the spectra. The full width half maximum (FWHM) for these peaks are about 3 kHz. Since the corresponding value for water

is about 0.54 kHz, this means that there is a negligible amount of adsorbed water on the sample surfaces. Both the FWHM and the hydrogen concentration (cm^{-2}) were similar to the results obtained from the thermally grown SiO_2 film [44]. Also, assuming a {100} monolayer of hydrogen on the pore surfaces (covered by $\text{Si}_2\text{-SiH}_2$), FWHM for the NMR peak can be calculated by using the Van Vleck formula:

$$FWHM = 189.6 \left(\sum_{j \neq i} r_{ij}^{-6} \right)^{1/2} \text{ (}\text{\AA}^3 \text{ kHz)} \quad (4.4)$$

where r = the inter-nuclear distance of protons (Angstroms). The calculation gives a FWHM about 41 kHz. This is much larger than the observed results. Therefore the sample surface are probably not covered solely by the static Si-H bonds of $\text{Si}_2\text{-SiH}_2$. Other configurations of Si-H bonds may be possible (e.g. $\text{Si}_3\text{-Si-H}$, $\text{O}_3\text{-Si-H}$, $\text{O}_2\text{Si-Si-H}$), so that the crystal structure close to the surface is disturbed, and the proton to proton distance may be larger than assumed. Another possible origin for the narrow FWHM is the Si-OH bonds on the surface, which can rotate more freely than the Si-H bonds, and hence the NMR signal will be averaged to a smaller FWHM. The approximate spin-lattice relaxation time (T_1) of the samples were about 3 s, which was in between the corresponding values of the freshly made and aged thermally grown SiO_2 films [44]. This information was important as it provided a measure for deciding the recycle delay being used in the ^{29}Si NMR by the cross polarization - magic angle spinning (MAS) method discussed in the next chapter.

Also, ^1H NMR had been applied to an aged PS sample which had been stored in air for about two months. The ^1H NMR signals normalized by the sample volumes are shown in figure 4.3. FWHM of the samples were about 2.5 kHz, a little bit less than before. No calibration were performed before the experiments, therefore the absolute data were not obtained. However, the relative intensities of the samples would remain more or less the same. It was found that the 25 mA sample had a much higher intensity than both the 100 mA and the 50 mA sample. In addition to that, the order of the intensity had changed as well. The 100 mA sample had a higher intensity than the 50 mA sample after two months. The change of relative intensity was probably related to the addition of protons from the air, since it had been found that oxidation of PS in air at about room temperature would not eliminate the Si-H bonds. Instead, oxygen was inserted between the Si-Si back-bond. With a smaller FWHM after two months, using the same argument as before, we could assume that

the addition of protons from the air might be partially taking place in the form of adsorbed water molecules on the surface.

4.4 ^{19}F NMR

^{19}F NMR on the aged PS samples were also performed by a home-built NMR probe. Teflon samples with different fluorine contents were used to build the calibration curve. Concentrations of ^{19}F measured in the samples were found to be below our detection limit of about 10^{17} nuclei (That is the inherent ^{19}F from the components in the probe.). This is consistent with the results from others. Although F^- ion is important in the overall reaction to produce PS, the intermediate product from the initial step, SiF_2 , is unstable and reacts further to form other products, and finally ends up as H_2SiF_6 . Therefore, it is not unreasonable to find few fluorine atoms on the PS surface.

4.5 Conclusion

In this chapter, ^1H NMR and the corresponding PL were measured for the PS samples made by Spire Corporation, MA, in order to investigate the possible correlation between the PL property and the surface chemistry of the material. Three samples were examined. They were processed under the same conditions with the exception of the anodization current density, which ranged from 100 mA/cm^2 to 25 mA/cm^2 . Compared with our samples processed in the similar situations, their samples had a much smaller thickness.

PL measurements of the samples showed that the trends in the intensity and the peak wavelength were not monotonic. However, such trends were not found in the corresponding ^1H NMR spectra, which were used to quantify the proton content in the samples. ^1H NMR showed that the content of protons decreased with the current density. The result was unexpected, as it had been known that a higher current density would lead to a higher surface area, and hence a higher proton content if a similar surface chemistry for all three samples was assumed. All these information indicated that, the Spire samples were different from the ones discussed in the last chapter, although they were made under similar conditions.

Although the chemical shift range in ^1H NMR was too small to resolve, from the FWHM of the ^1H NMR, it was still able to conclude that the source of hydrogen was not coming from the adsorbed water on the surface. Also, it showed that the surface was not

solely covered by $\text{Si}_2\text{-Si-H}_2$. Some other configurations for the Si-H bonding (e.g. $\text{Si}_3\text{-Si-H}$, $\text{O}_3\text{-Si-H}$), or other kinds of bonding like Si-OH that can rotate more freely, are needed to lower the FWHM to the measured value.

^1H NMR of the aged samples after two months were also performed. FWHM of them were ~ 2.5 kHz, a little bit less than before, and it was found that the proton contents in the samples had changed over time. The 25 mA sample had a much higher proton level than the other two samples. Also, after two months, the 100 mA sample had a higher proton level than that of the 50 mA sample. The reason for this was not certain, but it certainly shows the problem with reproducibility of the samples.

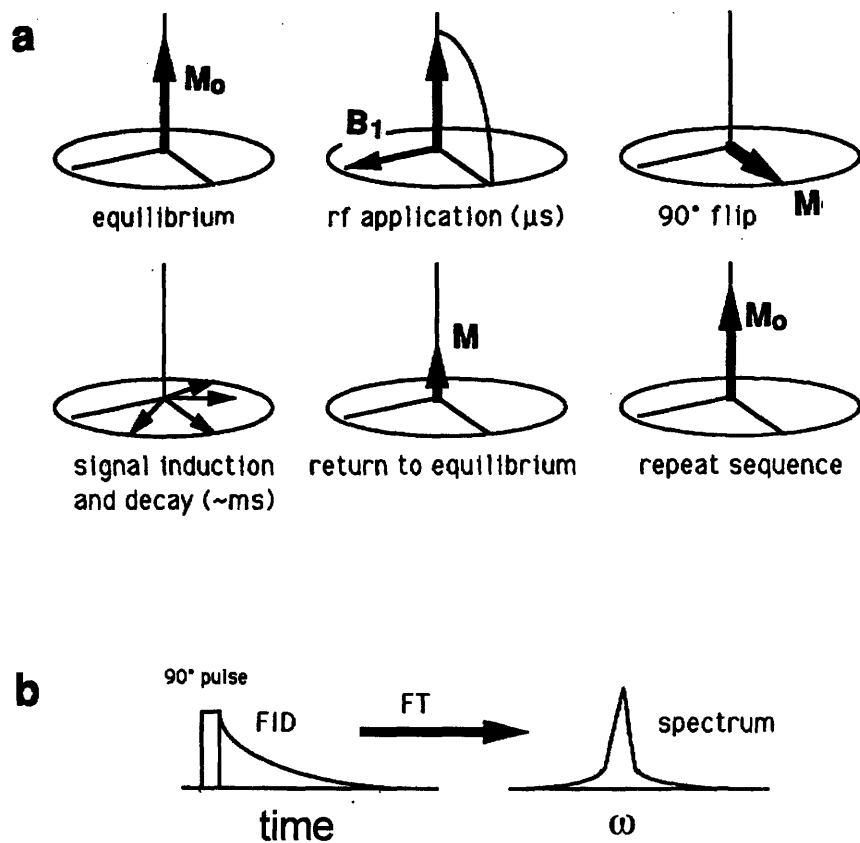


Figure 4.1 Schematic of NMR detection. a) Change of magnetization with time. b) free inductive decay and its fourier transform

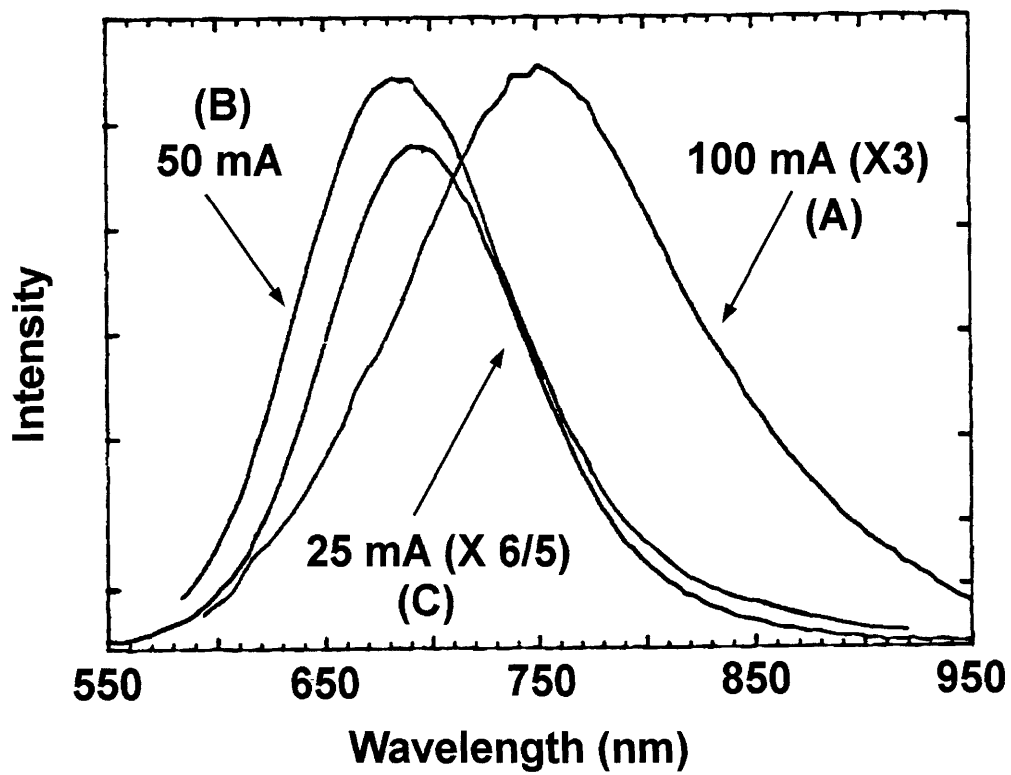


Figure 4.2 PL spectra of the freshly made PS samples from Spire Corporation. a) 100 mA; b) 50 mA; c) 25 mA;

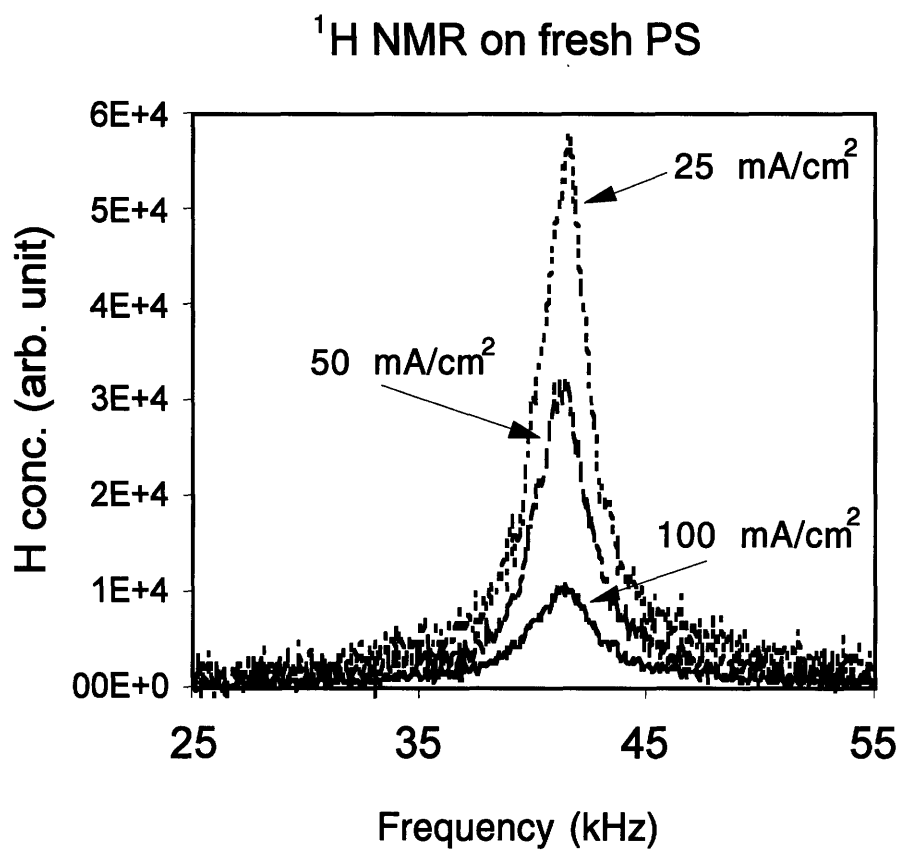


Figure 4.3 ^1H NMR spectra of the same three samples after normalization (fresh)

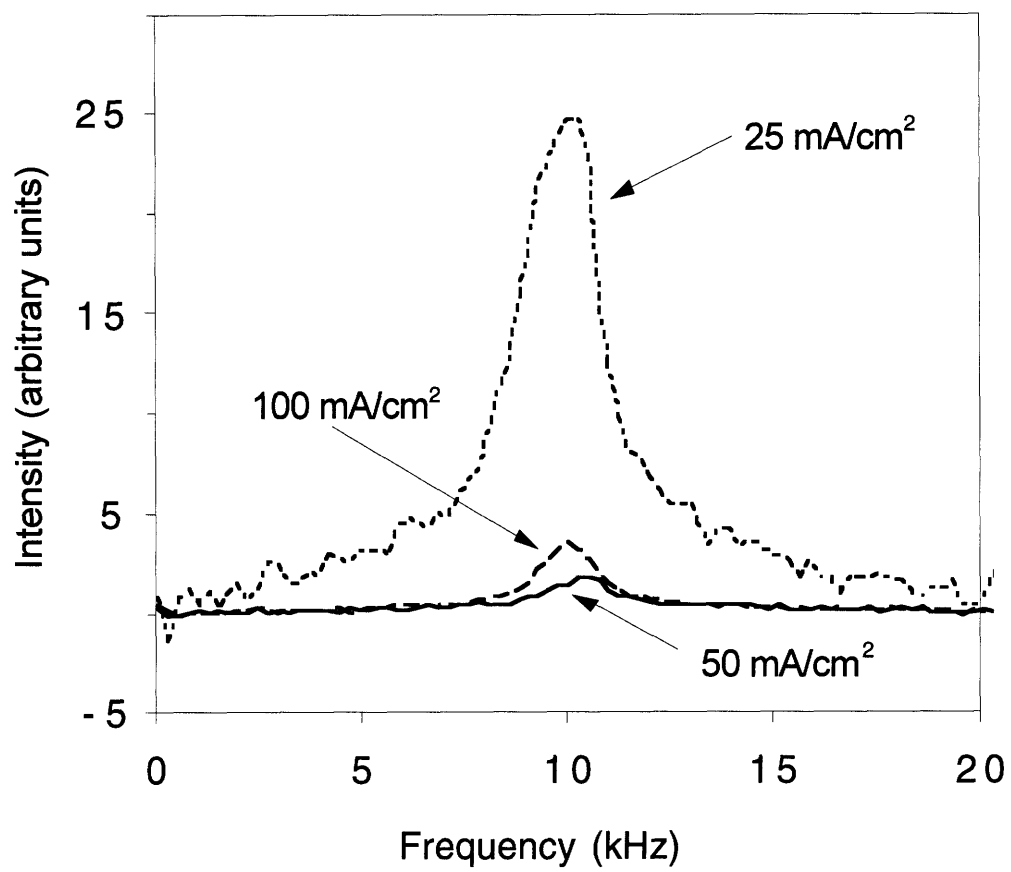


Figure 4.4 ¹H NMR spectra of the three samples after normalization (2 months later)

Chapter 5. Selective PS sample and their characterizations

5.1 Introduction

After obtaining the results of chapter 3, we were in a position to decide a suitable window for the anodization parameters. Wafers from set 3 (table 3.2) were used. In order to produce PS that was thick enough for examination, only those parameter values that yielded type B and type C PS were considered. Also, in order to achieve different PL intensities in the samples, parameters were chosen such that the resulting PS would cross the boundary between the type B (with observable PL) and type C (no/very weak PL) regions.

By studying the results from the previous experiments, the series which had been chosen for comparison had the following configuration: p-type Si wafers: 1-10 Ωcm ; HF concentration: 30 wt% ; current density: 20 mA/cm²; with a varying anodization time: 45 minutes, 60 minutes, and 90 minutes (sample 1, 2, and 3). According to the previous results [16], the pore size under this configuration would be ~ 100 Å, while the inter-pore distance would be ~ 50 Å. Two samples were made for each anodization time. One of the samples of each pair the PS layer remained intact on the wafer. It was made for the PL measurements. The other sample was a free standing layer, which was crushed into tiny pieces for the measurement of FTIR, BET and NMR. The thicknesses of sample 1, 2, and 3 were 55 ± 10 μm , 70 ± 10 μm , and 110 ± 10 μm respectively. Table 5.1 summarize the results:

Sample	Anodization time (minute)	Area (cm ²)	Thickness (μm)	Average etching rate ($\mu\text{m}/\text{min}$)
1	45	54.4	55	1.22
2	60	54.4	70	1.17
3	90	54.4	110	1.22

Table 5.1 Thickness and the anodization time of the final set of samples

The amount of HF consumed in the process was also calculated. From chapter 3, it is proposed that in the overall reaction, a Si atom reacts with 2 holes and 6 HF molecules. Therefore, a 1.01 A current leads to a supply rate of $1.05 \cdot 10^{-5}$ (moles of holes)/s, a consumption rate of $3.14 \cdot 10^{-5}$ (moles of HF)/s, and a removal rate of $0.52 \cdot 10^{-5}$ (moles of silicon)/s, which equals to $6.3 \cdot 10^{-5}$ cm³/s (density and atomic mass of Si crystal: 2.33 g/cm³

and 28.1 respectively). For the 45 minute sample, $6.3 \times 10^{-5} \times (45 \times 60) = 0.17 \text{ cm}^3$ of Si was removed, which equals 0.014 mole. On the other hand, 125 cm^3 of 48 wt% HF (density: 1.13 g/cm^3) in the 232 cm^3 electrolyte provides 3.34 moles (molecular weight of HF: 20.0) of HF in the electrolyte. As a result, only 2.5 % of HF was used during anodization. Similarly, in the 60 and 90 minutes samples, only 3.3 and 5.0 % of HF was consumed respectively. It shows that the HF concentration in the electrolyte is basically unchanged during the experiments.

Also, we were interested in the change of HF concentration in the PS layer. The Thiele modulus (Φ), which is an indicator for the concentration gradient in porous materials, was calculated in each experiment. When Φ was smaller than ~ 0.4 , the concentration of the reactant (HF) can be considered roughly constant along the pores. The formula of the Thiele modulus is [45]:

$$\Phi = L \sqrt{\frac{k}{D_{eff}}} \quad (5.1)$$

where L = characteristic length in the reaction = thickness of the PS layer in our case, k = rate constant for the consumption of HF, and D_{eff} = Effective diffusion coefficient of the reactant (HF) within the PS layer. $D_{eff} = \epsilon D / \delta$, where D is the bulk diffusion coefficient, δ is the tortuosity factor of the pores in PS, and ϵ is the volume fraction of PS. For the 45 minutes sample, $L \sim 55 \text{ }\mu\text{m}$, and $\delta \sim 1.41$ (detailed calculations are shown in the later part of the chapter). D was taken as $\sim 10^{-4} \text{ cm}^2/\text{s}$, a typical value for a liquid. The volume of the PS layer = area*thickness = 0.299 cm^3 . Therefore the volume fraction, ϵ , of the 45 minute sample was $0.17/0.299 \sim 0.57$. k was defined in the equation $-r = k C$, where r : rate of HF consumption per unit volume of PS and C : HF concentration. From the previous calculation, C was found to be $3.34/232 \sim 1.44 \times 10^{-2} \text{ mole/cm}^3$. Assuming a nearly constant etching rate ($\mu\text{m}/\text{min}$), the average volume (excluding the pores) of the PS layer during anodization = $(0.299 \times 0.57)/2 = 0.0868 \text{ cm}^3$. Therefore $-r \sim 3.6 \times 10^{-4} \text{ mole/cm}^3/\text{s}$. k was then calculated to be 0.025 /s , and $\phi \sim 0.136$, which is smaller than 0.4. As a result, we could conclude that the concentration of HF was nearly constant along the pores. Similarly, results for the 60 and 90 minute samples were also calculated. They are summarized in table 5.2

	45 minutes	60 minutes	90 minutes
Volume of the PS layer (cm ³)	0.299	0.381	0.598
Void fraction	0.57	0.59	0.57
Thiele modulus	0.163	0.175	0.293

Table 5.2 Thiele Modulus of the three PS samples

5.2 Photoluminescence Characterization Results

All PL measurements were performed in Prof. Kolenbrander's lab in the department of Materials Science of Engineering at MIT. The wavelength of the excitation laser was 355 nm. Samples had been made for about 2 months before the PL measurements, which were all performed under the same environment. Therefore, the resulting spectra intensity could be compared with confidence. The results are shown in figure 5.1. All samples have the same wavelength for their PL peaks at ~ 700 - 710 nm. The FWHM for sample 1, 2 and 3 are about 150 nm. Sample 1 had only a barely visible PL, PL from sample 2 was stronger, and the strongest one belonged to sample 3. That means that the PL intensities of these samples correlate to the anodization time of PS.

5.3 FTIR Characterization Results

FTIR measurements were performed in Prof. Jackie Ying's Lab in the Department of Chemical Engineering at MIT. Additional oxidized or reduced PS samples were also examined for comparison. The results of the three samples are shown in figure 5.2. They show that the PS samples with different anodization times have similar features in their surface chemistry. Generally speaking, they all have the same peaks in the FTIR spectra, although the relative intensities of these peaks vary somewhat. As discussed in several previous articles, the peaks at ~ 2090 cm⁻¹ and 2116 cm⁻¹ correspond to the stretching mode of the Si-H bond in Si₃-Si-H, Si₂-Si-H₂ respectively, while the peaks at 2195 cm⁻¹ and 2248 cm⁻¹ correspond to the same mode of the Si-H bond in SiO₂-Si-H and O₃-Si-H respectively [46, 47]. The peak at 2134 cm⁻¹ can be coming from either Si₂O-Si-H or Si-H₃ [48, 49, 50]. Both species have resonances around that wavenumber. The FTIR spectra show that all three samples were partially oxidized in air. The assignments of the peaks are summarized in table 5.3:

Wavenumber (cm ⁻¹)	Type	Mode
2248	O ₃ -Si-H	Si-H stretching
2195	O ₂ Si-Si-H	Si-H stretching
2134	OSi ₂ -Si-H or Si-H ₃	Si-H stretching
2116	Si ₂ -Si-H ₂	Si-H stretching
2090	Si ₃ -Si-H	Si-H stretching
986-1266	Si-O-Si	Si-O stretching
913	Si ₂ -Si-H ₂	Si-H scissor
806-940	Si-O-Si	Si-O bending
665	Si ₂ -Si-H ₂	Si-H bending/wagging
629	Si ₃ -Si-H	Si-H bending/wagging

Table 5.3 Assignments of the FTIR peaks in the PS samples

There are 3 blocks of peaks in the lower wavenumber range. The blocks from ~ 986 cm⁻¹ to ~ 1266 cm⁻¹ and from ~ 806 cm⁻¹ to ~ 940 cm⁻¹ are related to the stretching/bending modes of the Si-O bonds in groups mainly with Si-O-Si. The block from ~ 629 cm⁻¹ to ~ 665 cm⁻¹ is related to the wagging/bending modes of the Si-H bond in Si₃-Si-H and Si₂-Si-H₂ [50, 51]. Also, at around 913 cm⁻¹, there is another peak related to Si₂-Si-H₂. Although this peak is not easy to distinguish in the partially oxidized species, it will become more clear in the FTIR spectra of the reduced PS sample discussed later. This assignment can be further confirmed by comparing the FTIR spectra of the same sample (90 minutes) before and after annealing in air at $\sim 200^\circ$ C. This is shown in figure 5.3. The Si₃-Si-H and Si₂-Si-H₂ peaks at 2090 cm⁻¹ and 2116 cm⁻¹ from the stretching mode, and the 629 cm⁻¹ and 665 cm⁻¹ peaks from the wagging/bending mode disappear after oxidation. However, the ones related to O₃-Si-H and O₂Si-Si-H still remain. Furthermore, for those samples that have high FTIR intensity signals for the oxygen related peaks at 2195 cm⁻¹ and 2248 cm⁻¹ in the high wavenumber range, they also have strong signal intensities for the two oxygen related blocks at the low wavenumber range (figure 5.2).

Figure 5.2 also shows that in all three samples, the Si₃-Si-H and the Si₂-Si-H₂ species have roughly the same concentration on the PS surface. In addition, the O₃-Si-H peak is about half the intensity of the O₂Si-Si-H peak in all three samples. However, the ratio of the ‘unoxidized’ species and the ‘oxidized’ species varies. The sample after 90 minutes anodization is more oxidized than the others. However, the 45 and 60 minutes samples are

very similar to one another. The amount of $\text{OSi}_2\text{-Si-H}$ in the samples is difficult to determine as it overlaps with the $\text{Si}_2\text{-Si-H}_2$ and the Si-Si-H_3 peak.

The broad peak around $\sim 3000\text{ cm}^{-1}$ to $\sim 3700\text{ cm}^{-1}$ could be related to the OH groups that are bonded to the absorbed water on the pore surface, and the peak at 3734 cm^{-1} can be assigned as the one for the Si-OH groups [47, 52]. It has been found that all three samples in figure 5.2 have a smaller amount of OH on the surface compared with the annealed sample (figure 5.3), which also has a certain number of the Si-OH groups. However, the amount of Si-OH is outnumbered by the $\text{O}_3\text{-Si-H}$ and the $\text{O}_2\text{Si-Si-H}$. This indicates that oxidation of PS at room temperature in air tends to break the Si-Si back-bonds rather than the Si-H bonds, which agrees with previous work [9, 53].

Also, in certain spectra there are additional peaks at $\sim 2965\text{ cm}^{-1}$, $\sim 2860\text{ cm}^{-1}$, and $\sim 1267\text{ cm}^{-1}$. By comparing with the standard FTIR spectra of different type of silanes, it can be found that the peaks are probably related to the CH_3 groups on the PS surface. The intensities of these peaks increased when the samples were annealed in air inside the oven. The possible sources of these groups include ethanol that was used to dilute HF in the electrolyte, hydrocarbons from the air, and the remains of the evaporated vacuum oil in the annealing oven. Another feature that appears occasionally in the FTIR spectra was the group of peaks lying between $\sim 1400 - \sim 1900\text{ cm}^{-1}$, which were probably coming from water absorbed on the sample surface.

5.4 ^{29}Si NMR Characterization Results

The main reason for using ^{29}Si NMR is to investigate the chemical nature of the PS surface. Although proton NMR is more sensitive than ^{29}Si NMR, and hence easier to detect, the chemical shift of ^1H due to different chemical environments is so small ($< \sim 10\text{ ppm}$) that the peaks in the ^1H spectrum will be close together, and it is very hard to resolve one peak from another. On the other hand, ^{29}Si has a much wider chemical shift, so it can be easier to identify different peaks in the spectrum. Generally speaking, ^{29}Si NMR is even more insensitive than ^1H NMR as the natural abundance of ^{29}Si is only 4.7 %, while that of ^1H is close to 100 %. However, the sensitivity of ^{29}Si NMR can be enhanced by the Cross Polarization - Magic Angle Spinning (CPMAS) technique.

To assist the analysis of the spectra, additional oxidized and reduced PS samples were examined for comparison. The third sample, which had been anodized for 90 minutes in HF, was divided into two parts. The first part was oxidized in air at $\sim 200^\circ \text{C}$ for about 4 hours. After NMR and FTIR measurements were taken from the sample, it was further oxidized for about 60 hours at the same temperature, and the corresponding changes in NMR and FTIR were compared. The second part of the sample was reduced by soaking it in HF for 10 minutes, followed by drying in air without being washed by water. NMR measurements were taken immediately after the treatment in order to minimize any signal originating from the oxidation of the sample in air. FTIR of the same sample was taken after the NMR characterization.

^{29}Si NMR was performed by the Cross Polarization - Magic Angle Spinning (CPMAS) method. In the cross polarization part, a sequence of excitation pulse are used such that 1) a high magnetization is built up for the proton on the PS surface; 2) a mechanism is established through the "contact" of the protons and the surface Si atoms to transfer the magnetization from the protons to silicon atoms, with the transfer rate $\propto r^{-6}$ (r : distance between proton and silicon); 3) silicon magnetization was measured, like ordinary NMR. As described in the procedure, only the Si nuclei close to the surface can be influenced by the protons. Therefore it provides a way to differentiate the properties of the surface Si atoms from the that in the bulk. Also, since the recycle delay is mainly determined by the build up of proton magnetization in step 1), the shorter T_1 of proton means more signal averages can be performed in a given time, and an improved sensitivity for the ^{29}Si NMR in a practical sense. The cross polarization time in our experiments was 3 ms. For the MAS part, the sample is spinning around a symmetry axis which makes an angle $\phi = 54.7^\circ$ with the external magnetic field, B_0 , from the magnet. Since the dipole-dipole interaction $\propto 3\cos^2\theta-1$ (θ = the angle between B_0 and the inter-nuclear vector), when the spinning of the sample is fast enough, the average of $3\cos^2\theta-1$, $\langle 3\cos^2\theta-1 \rangle$, will be proportional to $3\cos^2\phi-1 = 3\cos^2(54.7^\circ)-1 = 0$. However, in real situations, the dipole-dipole interactions are usually too large for the above condition to be valid. Nevertheless, the use of MAS will still improve the narrowing of the spectra. Also, the chemical shift anisotropy (CSA) includes a term $(3\cos^2\phi-1)$, where ϕ = the angle between B_0 and the principle axis of the chemical shift tensor. By the same analogy, MAS will also suppress CSA, and only the isotropic chemical shift will be detected. In our experiments, the PS samples were spinning with a frequency $\sim 2900 \text{ Hz}$. The 90° pulse time was $4 \mu\text{s}$. The ^{29}Si resonance frequency was 53.64 MHz . The dipolar decoupling time was 10 ms. The recycle delay time was 40 s. All spectra recorded were plotted in ppm from the tetramethylsilane (TMS) reference. The NMR spectra of the three samples with anodization

time 45, 60 and 90 minutes are plotted in figure 5.4. It shows that chemically the three samples were similar, in agreement with the FTIR results. Only the ratios of the different species has changed. The spectrum can be roughly identified in 2 regions. The first one is a relatively sharp peak centered at ~ -50 ppm, with FWHM ~ 6 ppm. The next one is a broad region ranging from ~ -80 ppm to ~ -110 ppm. There is heavy overlapping of several peaks under this region and more has to be done to resolve the spectra. Figure 5.4 shows that the 45 minute and the 60 minute samples were similar, while the 90 minute sample is much different (in terms of the intensities of the peaks). This feature is also found in the FTIR spectra of the three samples (figure 5.2). The difference may be due to the handling of the samples after they were made (for example, the washing of PS by distilled water), as it is known that the properties of PS is very sensitive to the surrounding environment.

The chemical shift of the NMR signals is related to the electronic screening around the silicon nucleus, which depends on the type, the number, and the relative positions of the surrounding atoms. Both the nearest neighbors and the second nearest neighbors can affect the chemical shift [54]. Generally speaking, the more electronegative the surrounding atoms are, the less electronic screening around the Si atom, which will shift the resonance to a higher frequency. In the CPMAS experiment, the chemical shift (δ) is related to the average isotropic value of the electronic screening tensor (σ) around the nucleus created by the surrounding atoms and can be calculated according to the following equation:

$$\nu = \frac{\gamma}{2\pi} (1 - \sigma) B_0 \quad (5.2)$$

$$\delta = \sigma_{\text{ref}} - \sigma \quad (5.3)$$

where ν = resonance frequency, γ = magnetogyric ratio (nucleus specific), σ_{ref} = electronic screening tensor of the reference (TMS in this case), and B_0 is the external magnetic field (6.3 T in this case).

From the previous experimental results of ^{29}Si in the solution system [55, 56], silica system [57], and the amorphous silicon (a-Si) system [58, 59], it can be found that 1) the isotropic chemical shift is approximately linear with the sum of electronegativities of the nearest neighbors; 2) replacing the hydroxyl group (-OH) by the bridging oxygen (-Si-O-Si-) in the SiO_2 system around the silicon atom will shift the resonance frequency by ~ -10 ppm; 3) replacing Si by H on the surface (Si-H to Si-H₂) of the a-Si system will shift the resonance frequency to a lower level (more negative) [59].

^{29}Si NMR of the original silicon wafer (10 Ωcm), which was the starting material for the three samples, was also performed by direct polarization, with a recycle delay of 60 s. Powder sample (by grinding the wafer) was used. 20 accumulations were added to give the spectrum, which is shown in figure 5.5. The chemical shift of pure Si of such resistivity was found to be ~ -81 ppm relative to the tetramethylsilane (TMS) standard with a small FWHM ~ 2 ppm. This is consistent with the other results [60].

^{29}Si CPMAS results of the two oxidized PS are shown in figure 5.6. They show that the most significant changes brought by oxidation had taken place after 4 hours at 200° C. Further oxidation brought only changes in the intensities of the existing peaks, but no additional peaks were created or destroyed. Comparing with figure 5.4, the peaks at about -50 ppm, -84 ppm and -109 ppm still exist, but the region around -100 ppm has dropped rapidly. The corresponding FTIR spectra (figures 5.7) confirm that the main oxidized features have already been established after 4 hours of annealing: 1) around 2000 - 2200 cm^{-1} , most of the $\text{Si}_3\text{-Si-H}$ and $\text{Si}_2\text{-Si-H}_2$ species have disappeared, and the main components remain in that region are $\text{O}_2\text{Si-Si-H}$ and $\text{O}_3\text{-Si-H}$. 2) in the low wavenumber region (~ 1000 cm^{-1}), there are strong signals from the Si-O stretching/bending modes of Si-O-Si; 3) in the higher wavenumber region (~ 3734 cm^{-1}), there is a small amount of Si-OH groups; 4) around 3000 cm^{-1} , there are signals coming from the O-Si- CH_3 groups; Compared with the NMR results in figure 5.6 it can be certain the three peaks at -50, -84, and -109 ppm are related to the oxygen containing groups (that is, $\text{O}_2\text{Si-Si-H}$, $\text{O}_3\text{-Si-H}$, SiO_2 groups close to the surface, and the O-Si- CH_3 groups).

Figure 5.8 shows the NMR and FTIR results of the PS sample 3 which was reduced in HF. The NMR spectrum, which consists of a wide block from ~ -75 ppm to ~ -115 ppm, centered at ~ -100 ppm, shows that the oxygen related species (~ -50 ppm and ~ -84 ppm) have disappeared on the PS surface. The FTIR counterpart shows that this wide block is mainly composed of $\text{Si}_3\text{-Si-H}$ and $\text{Si}_2\text{-Si-H}_2$ with a little $\text{Si}_2\text{O-Si-H}$ or Si-Si-H_3 . It also shows that PS directly from HF does not contain any $\text{Si}_n\text{O}_{3-n}\text{-Si-OH}$ (~ 3734 Hz) species. That means the $\text{Si}_n\text{O}_{3-n}\text{-Si-OH}$ groups found in the untreated PS is probably coming from oxidation by the absorbed water after they were made.

In addition CPMAS, polarization inversion technique was also used to help to identify different species under the broad peaks [61]. The experiments started in the same ways as the ordinary CP experiments did. However, after the first CP had been achieved, a second CP

(which had an opposite direction to the first one) was used to convert the NMR signals to the negative directions, and the rate of this inversion would reflect the distance between the Si atom and the hydrogen atom of different NMR peaks. In figure 5.9, ^{29}Si NMR spectra of the same sample with different polarization inversion times up to 960 μs were shown after the first CP contact time of 3 ms. It can be seen that different peaks are inverting at different rates. The closer the hydrogen to the Si atom in a species, the faster the corresponding peak will flip. Figure 5.9 shows that the peak at ~ -50 , -84 , and -102 ppm are among the ones with the highest flipping rate. The peak around ~ -91 ppm was flipping at an intermediate rate, and the peak at ~ -109 ppm is the slowest among all of them. Therefore it can be deduced that the peaks at -50 , -84 and -102 ppm are probably related to the species that are directly bonding with hydrogen. On the other hand, the slow flipping rate for the species at ~ 109 ppm indicates that hydrogen is further away from the Si atom in that species. Comparing with the chemical shifts data obtained from others, the peak at ~ -109 ppm is found to correspond to SiO_2 which are close to the surface [54, 57].

As the peak at ~ -109 ppm is identified as SiO_2 , from the previous FTIR and NMR results of the oxidized PS, it can be deduced that the peak at -84 ppm should correspond to $\text{O}_3\text{-Si-H}$, while the peak at -50 ppm may be related to the $\text{O}_2\text{Si-Si-H}$. This assignment is consistent with the fact that these two peaks were among the ones with the highest inversion rate in the polarization inversion experiment, and it is also consistent with the FTIR result of the oxidized PS, which shows the dominance of the $\text{O}_3\text{-Si-H}$ group over the $\text{O}_2\text{Si-Si-H}$ group in the sample.

As mentioned above, the polarization inversion experiment also shows another fast flipping peak at about -102 ppm. Combining with the NMR spectra of the reduced PS, it can be deduced that the peak at -102 ppm can be one of the following: $\text{Si}_3\text{-Si-H}$, $\text{Si}_2\text{-Si-H}_2$, or Si-Si-H_3 . Since the inversion rate increases with the number of hydrogen attached to Si, the peak at -102 ppm has a higher probability to be either $\text{Si}_2\text{-Si-H}_2$ or Si-Si-H_3 . FTIR of the same sample shows that there is much more $\text{Si}_2\text{-Si-H}_2$ than Si-Si-H_3 (if there is any). Therefore, the peak at ~ -102 ppm is more likely to be $\text{Si}_2\text{-Si-H}_2$. As a result, the remaining part of the spectra around -91 ppm is assumed to be $\text{Si}_3\text{-Si-H}$. This assignment is consistent with the result that Si-H_2 has a more negative chemical shift than Si-H [59], and it is also consistent with the -81 ppm peak for the bulk Si, which implies a roughly -10 ppm shift by replacing a Si atom by proton. However, compared with these assignments of the oxygen related peaks in the previous paragraph, there is contraction. If we assume that the change of the chemical shift is approximately linear with the replacement of one atom by the other, which implies

that Si₃-Si-H (~ -91 ppm) should have a higher chemical shift (less negative) than both O₃-Si-H (~ -84 ppm) and O₂Si-Si-H (~ -50 ppm). This contradiction may be solved if we assume that the chemical shift is a non-linear function of the sum of the electronegativities of the surrounding atoms, which is true for solutions [56], and might still hold in solids.

5.5 Morphology Results

Besides using electron microscope, the morphology of PS were also measured by physical adsorption and desorption. Surface area was measured by the Brunauer-Emmett-Teller (BET) method and the Barret-Joyner-Halenda (BJH) method [62], while the pore size distribution was measured by BJH (and desorption). Samples were sent to Micromeritics, GA, where these measurements were performed at room temperature, using N₂ as the probe.

In BET, the volume of nitrogen adsorbed at equilibrium on the sample surface is measured as a function of the applied nitrogen pressure at its boiling point (77 K). By extending the Langmuir isotherm to multilayer adsorption, the surface area can be determined from the measurement. Assuming non-intersecting straight pores, the average pore diameter can be estimated as well (later part in this section). However, BET does not provide direct data on the pore diameter distribution.

Pore diameter distribution can be obtained by BJH. The first stage of the BJH measurement is similar to BET. However, in BJH, the nitrogen pressure continues to increase until the adsorbed N₂ films start to bridge the pores [63]. Further uptake of nitrogen will result in capillary condensation, which will begin from the smallest pores and then extend to the larger pores. Therefore, the pore size distribution can be obtained by monitoring the change of the adsorbed nitrogen volume. After all the pores are filled with nitrogen, the pressure is decreased slowly, and the whole process will be reversed. Nitrogen molecules will start to evaporate from the largest pores first, and then extend to the smaller pores. In this case, the pore size distribution can also be measured.

Surface area, pore volume, and pore diameter distribution of the three PS samples with anodization time 45, 60 and 90 minutes were shown in table 5.4. The pore diameter distribution of the samples are shown in figure 5.10.

Of the two types of BJH measurements, usually it is the desorption data that are used. This is because during the adsorption process, the pores that have narrower openings than the pore diameters may inhibit the flow of nitrogen molecules into the pores and result in smaller measurements than the actual case. (table 5.4) On the other hand, in the desorption process, the "openings" of those pores had already been widened during adsorption, and therefore it provided more accurate measurements.

	Sample 1 (45 min)	Sample 2 (60 min)	Sample 3 (90 min)
Surface area, S (m ² /g) (BET)	424.0	739.8	564.2
Surface area, S (m ² /g) (BJH adsorption)	581.4	1085.3	892.7
Surface area (m ² /g) (BJH desorption)	688.8	1223.9	1024.6
Total Pore Volume, V (cm ³ /g) (BJH adsorption)	0.87	0.92	0.98
Total Pore Volume, V (cm ³ /g) (BJH desorption)	0.92	1.02	1.04
Pore diameter, d (Å) (calculated by BET, BJH adsorption)	82	50	68
Pore diameter, d (Å) (measured by BJH desorption)	58	34	42
Tortuosity factor, δ	1.41	1.47	1.62

Table 5.4. Morphologies of PS measured by physical adsorption and desorption

Figure 5.10 shows that the pore size distribution is monodisperse in the samples (that is, no bimodal distribution arising from the side pores of distinctly different size than the main pores). This is consistent with the p-type PS whose "main" pores can hardly be distinguished from the side branches. The average size of the pores can be calculated by the formula derived from simple geometry [62]:

$$d = \frac{4V}{S} \quad (5.4)$$

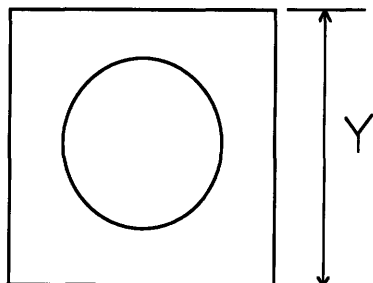
where d = diameter of the pore, V = total volume of the pore, and S = surface area of the pore, under the assumption that the pores are straight down from the top to the tip. From

the BET surface area and the BJH adsorption pore volume, the calculated pore diameter for the 45 minutes sample is $\sim 82 \text{ \AA}$. While the measured pore diameter is 58 \AA , the tortuosity factor, δ , (which is the measure of the effective length of the pore) of the 45 minutes sample is $82/58 = 1.41$. That means the effective length of the pore (x') is 1.41 times of the length (x) assumed in the simple straight cylindrical pore model, which is 55 \mu m in the 45 minutes sample. δ for the 60 and 90 minutes sample was calculated to be 1.47 and 1.62 respectively.

In the beginning of this chapter, it was found out that $\sim 0.17 \text{ cm}^3$ of Si was removed in the 45 minutes sample. Since the volume of the PS layer $\sim 0.299 \text{ cm}^3$. There was $\sim 0.299 - 0.17 = 0.129 \text{ cm}^3$ left in the PS layer, which was equivalent to $\sim 0.30 \text{ g}$. Therefore the calculated pore volume per gram of the sample was $\sim 0.17/0.30 = 0.56 \text{ cm}^3/\text{g}$. The corresponding result for the 60 and 90 minutes sample was 0.60 and $0.54 \text{ cm}^3/\text{g}$. They were about 55 % of the measurements in table 5.4. Considering the uncertainties involved in the calculation of these values, the difference is still acceptable.

Also, thickness of the wall between two pores had been estimated from the above data. The volume of each pore, $V_p = (d^2/4)\pi(x\delta)$. This equals to $2.05 \cdot 10^{-15} \text{ cm}^3$ in the 45 minute sample. Therefore the number of pores in the sample $n = V/V_p \sim 4.2 \cdot 10^{14} / \text{g}$ of PS. Assuming the pores were even distributed in a 1 gram block with dimension $Z \cdot Z \cdot x$, a mass balance equation can be set up as: $(Z^2x - V) \cdot 2.33 = 1$. For the 45 minutes sample, $x \sim 55 \text{ \mu m}$, $V \sim 0.87 \text{ cm}^3$, $Z \sim 15.4 \text{ cm}$. The distance between the centers of two pores, L_{p-p} , can be approximated by $Z/(n^{0.5})$, which is $\sim 75 \text{ \AA}$. As a result, the thickness of the wall between two pores $\sim 75 - 58 = 17 \text{ \AA}$. From similar calculations, V_p for the 60 and the 90 minute samples was calculated to be $9.34 \cdot 10^{-16}$ and $2.47 \cdot 10^{-15} \text{ cm}^3$, and the wall thickness was ~ 10 and 14 \AA respectively.

The wall thickness had been estimated in a second way. Assuming each pore is surrounded by a square block with dimension $Y \cdot Y \cdot x$, a top view of the block is shown in the figure:



The volume of the block is Y^2x , and the volume of the pore is $(d^2/4)\pi(\delta x)$. From the porosity of the sample, Y could be calculated. The porosity of the 45 minute sample ~ 0.57 . Therefore, $0.57Y^2 = (d^2/4)\pi\delta$ and $Y \sim 81 \text{ \AA}$. The wall thickness could then be found by $Y-d = 81-58 = 23 \text{ \AA}$. Similarly, the wall thickness for the 60 and 90 minute samples calculated by this method was ~ 14 and $\sim 21 \text{ \AA}$. Comparing with the corresponding values determined by the previous methods, it was found that they were generally consistent with each other. The results of these calculation are summarized in table 5.5

	45 minutes	60 minutes	90 minutes
Volume of each pore, V_p (cm^3)	$2.05 \cdot 10^{-15}$	$9.34 \cdot 10^{-16}$	$2.47 \cdot 10^{-15}$
Number of pores, n (/g)	$4.2 \cdot 10^{14}$	$9.85 \cdot 10^{14}$	$4.0 \cdot 10^{14}$
Z (cm)	15.4	13.9	11.3
Center to center distance, L_{p-p} (\AA)	75	44	56
Wall thickness (first method) (\AA)	17	10	14
Y (\AA)	81	48	63
Wall thickness (second method) (\AA)	23	14	21

Table 5.5 Estimation of the inter-pore wall thickness of the three PS samples

Several observations can be made from the data. First, the pore volume increases slightly as the anodization increases. Combined with the fact that the etching rate of the three samples were roughly constant, it can be assumed that the porosity (density) of the samples were similar. Second, sample 2 has the highest surface area, which is more than $\sim 30\%$ higher than the rest of the samples. Combining these two results, from the data it can be expected that the pore size will have a reverse trend to the surface area, and that is what is observed experimentally. All this information is consistent with the description of the pore formation mentioned before in the previous chapter: when anodization starts, more side branches start to grow from the original pores, which grow downwards towards the bulk of the Si wafer. However, the new branches are smaller than the original one from which they grew. Therefore while the surface area increases, the overall porosity is kept approximately the same. This describes the trend from sample 1 (45 min) to sample 2 (60 min), and implies that the inter-pore distance will decrease with time. Although the widths of the depletion region around the pores will set a minimum value for the inter-pore distance electrochemically, pure chemical etching of the pores ($< 1 \text{ \AA}/\text{min}$, much slower than the

electrochemical etching, which is in the order of 1 $\mu\text{m}/\text{min}$) can still occur. As a result, the top part of the pore will be wider than that close to the tip, as they are subject to a longer chemical etching time [16]. This explains the slight increase of the pore volume with anodization time (Table 5.4). Also, it implies that when the anodization time continues to increase, the pores will eventually start to meet and, the 'wires' in between the pores will then be either etched away or collapse. These contribute to the decrease of the surface area and the increase of the 'pore size' in sample 3 (90 min). If the anodization time is too long. The 'wires' will be too thin to support themselves mechanically, and break down under the capillary force, like what had been discussed before in the previous chapter. Note that in this process, although the change of the surface area and the pore size are not monotonic, the volume in between the pores is decreasing continuously. This is consistent with the quantum confinement explanation of the origin of the photoluminescence in PS [4], which intensity is also found to increase with the anodization time continuously in figure 5.1. Although the calculated wall thickness does not show this trend, the uncertainties involved in the calculation are large enough to take care of that. The most important information of this calculation is to get the idea of the wall thickness in the sample, which is found to be in the range that can induce quantum confinement effect.

5.6 Conclusion

FTIR measurements of the oxidized and the reduced PS have been done. They are consistent with the results of previous work, which stated that freshly made PS is mainly covered by $\text{Si}_{4-x}\text{-Si-H}_x$, and oxidation of PS in air at low temperature is mainly taking place by breaking the Si-Si back-bond, rather than the Si-H bond. Combining this with the corresponding ^{29}Si NMR measurements, the ^{29}Si NMR spectra of PS had been partially resolved, which was the first time this material was examined by ^{29}Si NMR. Using CPMAS method, the signal from the PS surface can be distinguished from that in the bulk, which corresponds to a sharp peak at ~ -81 ppm. Comparing the results of the oxidized and the reduced samples, peaks that are associated with oxygen have been revealed. The two largest ones are at ~ -50 and ~ -84 ppm. On the other hand, the peaks which are associated with hydrogen only were centered at ~ -100 ppm. From the inverse polarization technique, the relative distance between the hydrogen and the silicon atom in different species has been obtained, and it further enhances the understanding of the NMR spectra. Although not every peak was identified, uncertainties in the identification have been greatly reduced.

FTIR and NMR of the three samples showed that they were not very different, especially between sample 1 (45 min) and sample 2 (60 min). The difference in sample 3 could be due to the handling of the sample after it had been made, but the real reason was not certain. FTIR and NMR results of sample 1 and 2 were shown in figure 5.11 for comparison. However, it was found that the PL intensity of sample 2 was much higher than that of sample 1 (figure 5.1). This indicated that the PL origin is not pure chemically related, and favors the quantum confinement explanation (or its modifications) of the PL origin. The blues shift of PL predicted by this theory is further confirmed by the fact that both PL wavelengths of our samples are lying in the visible region, rather than the infra-red region from the bulk silicon. Although it is hard to say whether there is any blue shift between the 45 min and the 60 minute samples, an obvious blue shift is found between the 60 and the 90 minute samples.

Morphology measurements of the three samples show that their pore volume (cm^3/g) was similar. Combining this with the fact that the thickness of the PS layers grew roughly linearly with the anodization time, it could be deduced that the porosity of the three samples were similar. Furthermore, it was found that the surface area (m^2/g) first increased with the anodization time, and then dropped. These results could be explained by the assumptions that 1) the diameters of the new pores decreased while they branched out from the original pore, and 2) both the electrochemical and chemical etching processes were important in the anodization process, which could also lead to the explanation for the increase of the PL intensity with the quantum confinement model.

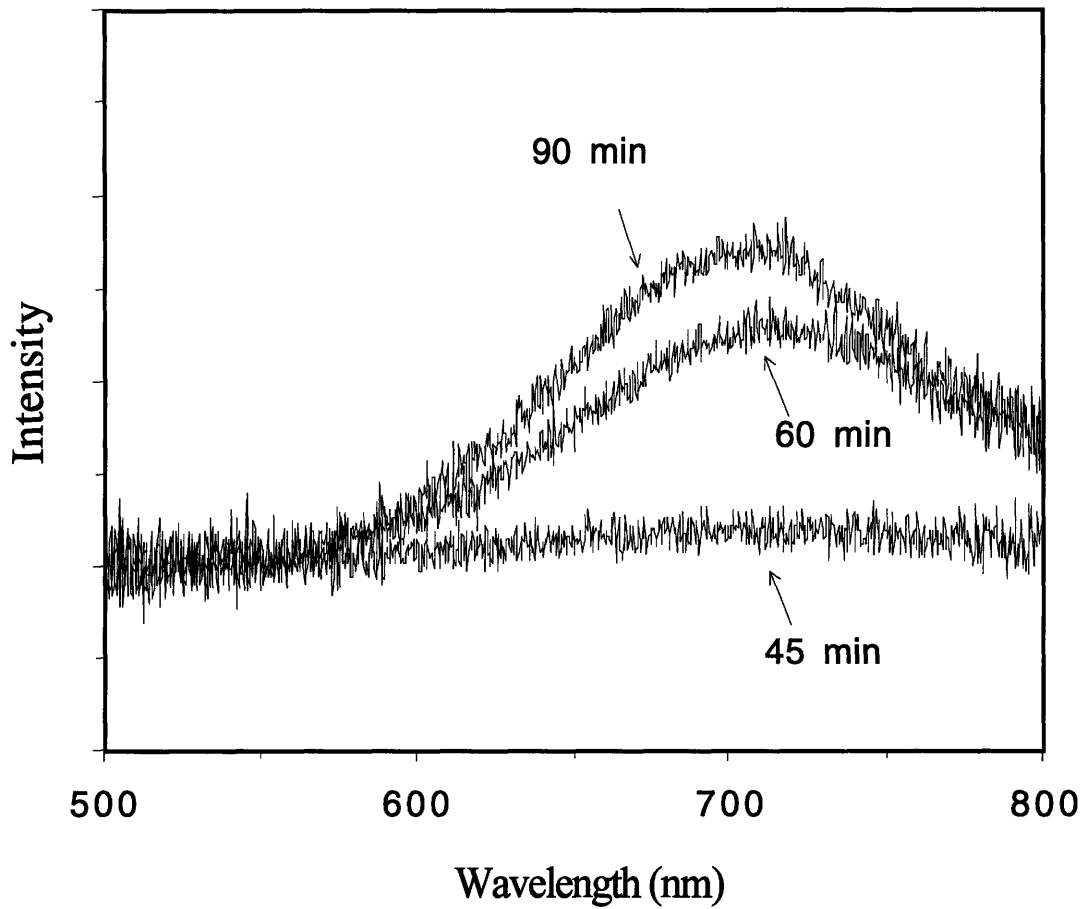


Figure 5.1 PL results of 3 samples anodized for different times: a) 45 min b) 60 min c) 90 min. Current density: 20 mA/cm², HF conc: 30 wt%

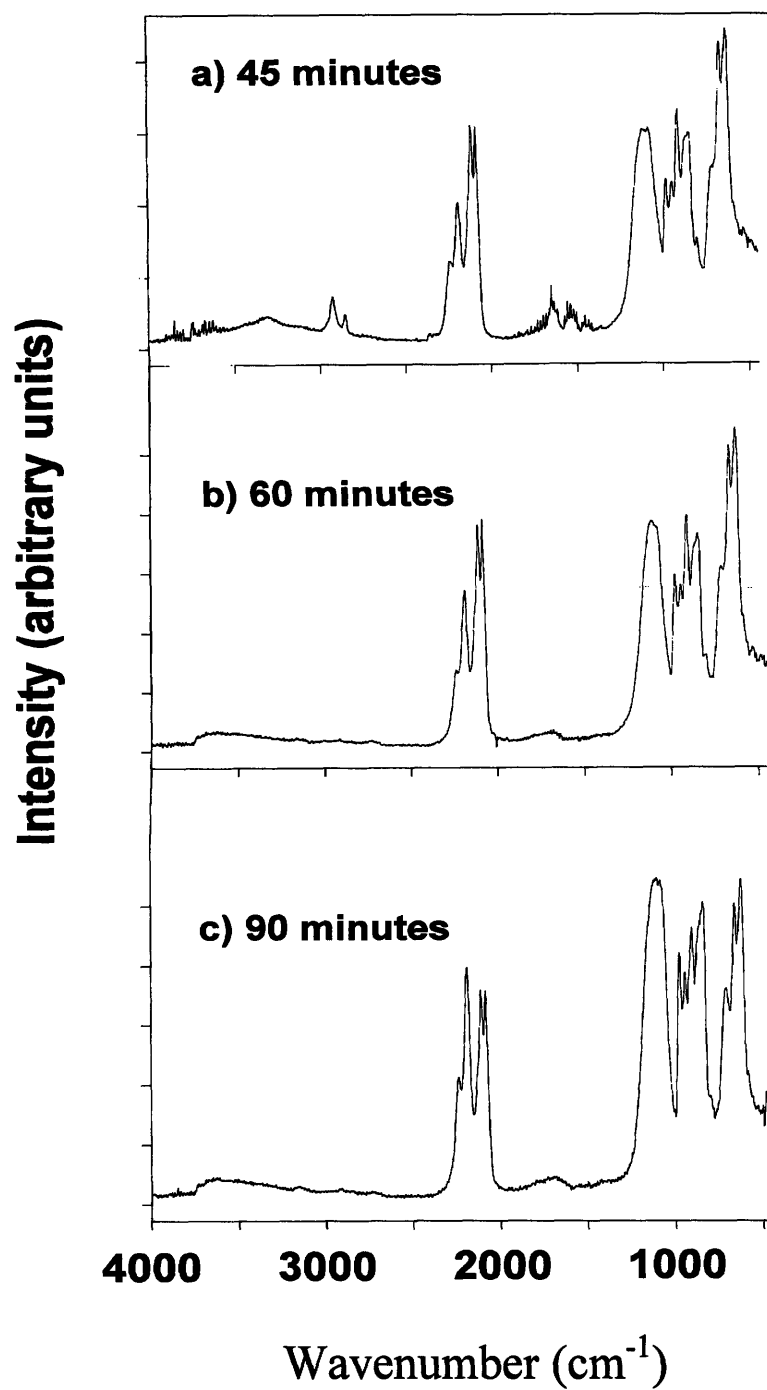


Figure 5.2 FTIR Spectra of 3 samples anodized for different times: a) 45 min b) 60 min c) 90 min. Current density: 20 mA/cm², HF conc: 30 wt%

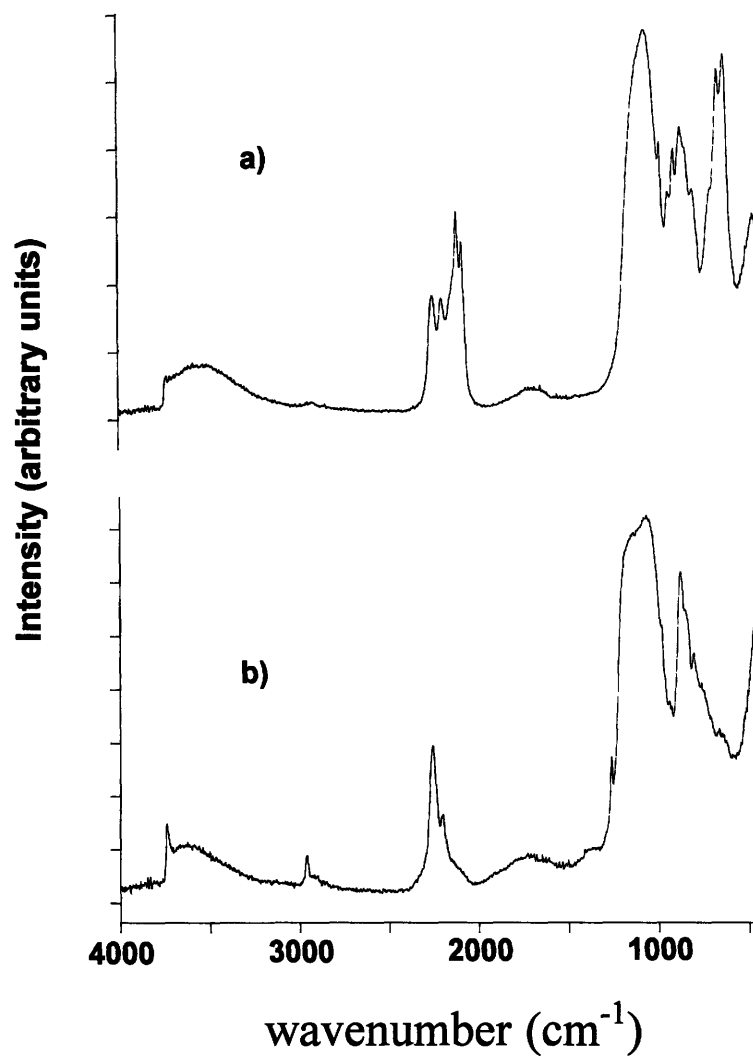


Figure 5.3 FTIR Spectra of the 90 minutes sample a) before and b) after annealing at ~ 200° C

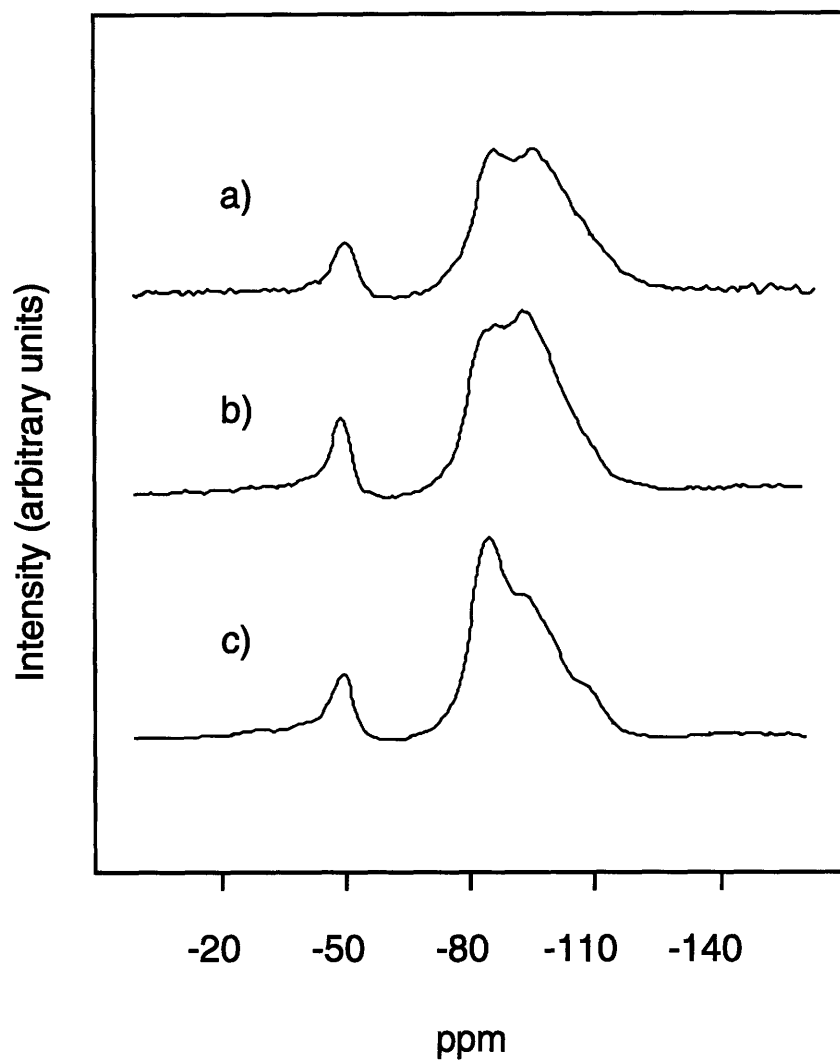


Figure 5.4 ^{29}Si NMR (CPMAS) results for 3 samples with different anodization time: a) 45 min b) 60 min c) 90 min. Current density: 20 mA/cm²; HF conc: 30 wt%; contact time: 3 ms; 1696, 512, 1000 signal averages respectively.

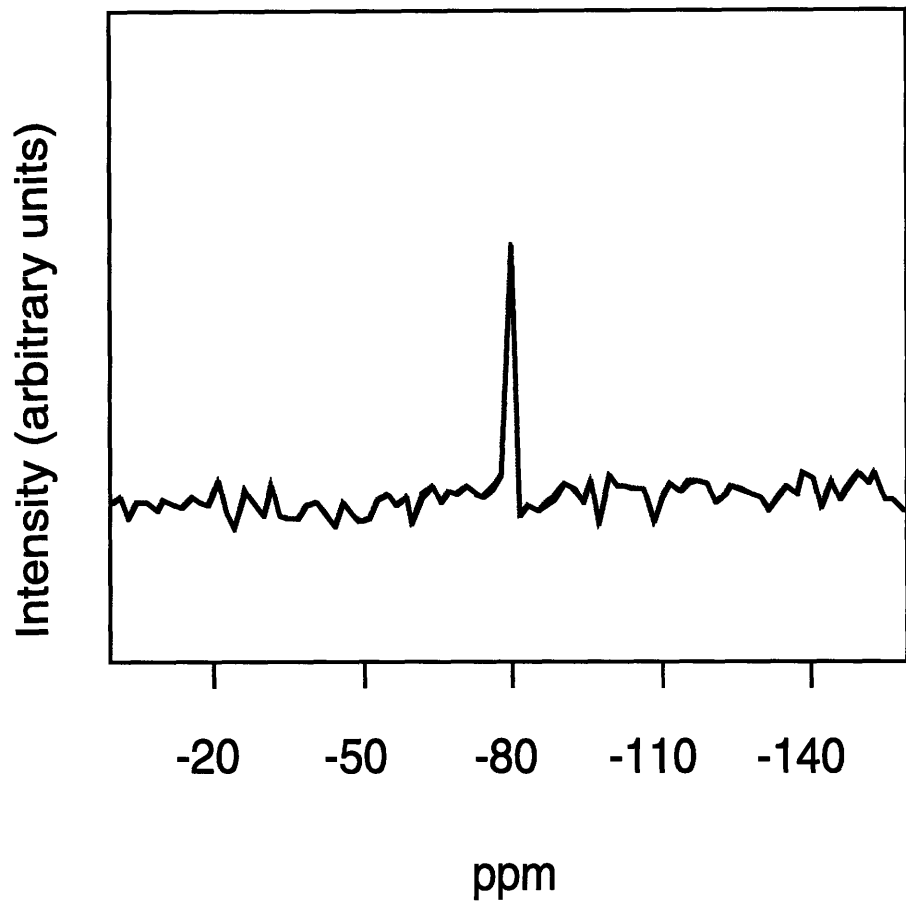


Figure 5.5 ^{29}Si NMR result of pure Si (20 signal averages)

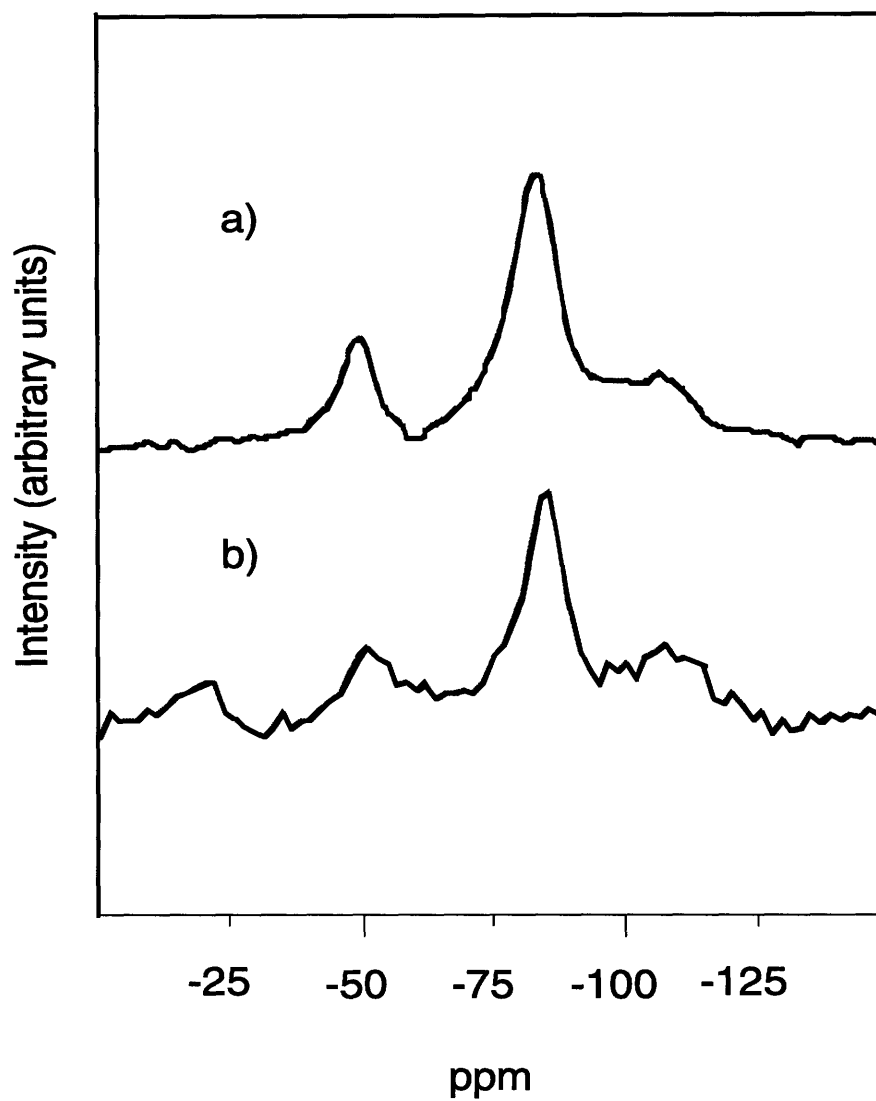


Figure 5.6 ^{29}Si NMR of two oxidized PS in air at $\sim 200^\circ\text{C}$: a) ~ 4 hours; b) ~ 60 hours;

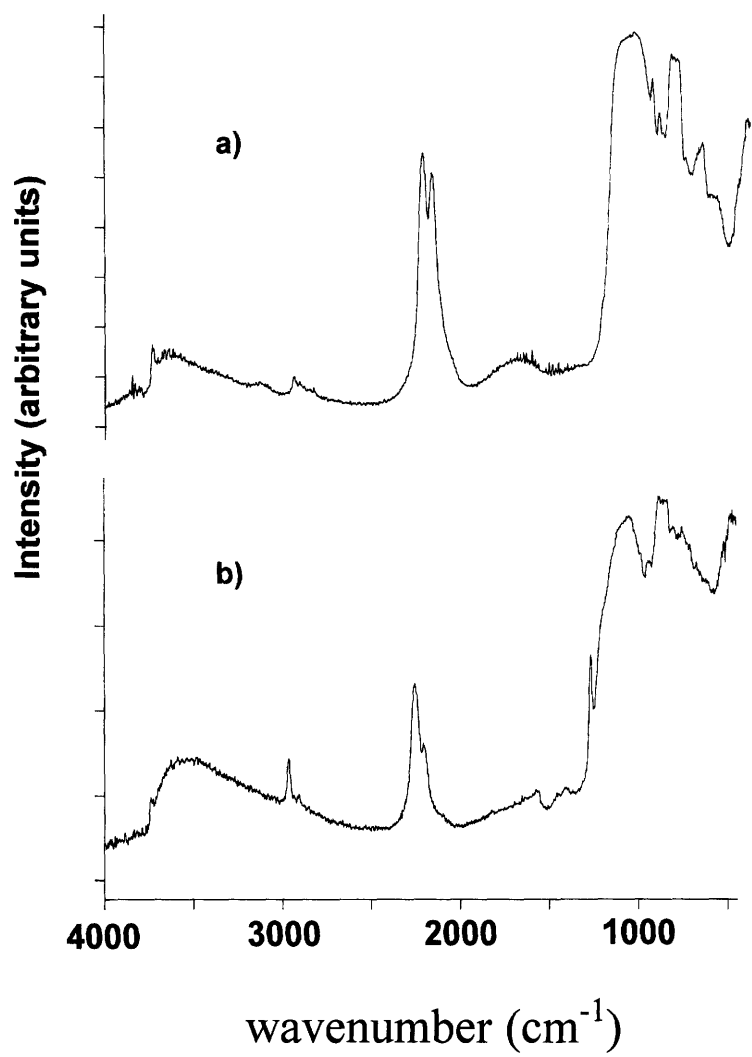


Figure 5.7 FTIR of two oxidized PS in air at $\sim 200^\circ\text{C}$: a) ~ 4 hours; b) ~ 60 hours;

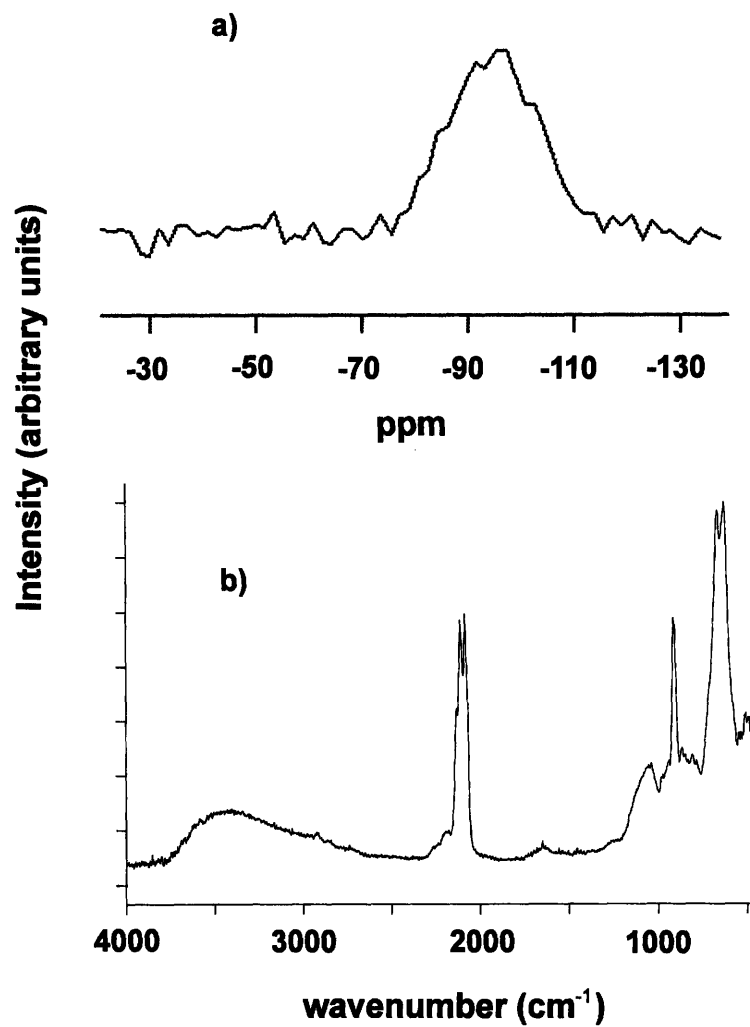


Figure 5.8 For the 90 minutes PS sample reduced in HF: a) ^{29}Si NMR, and b) FTIR;

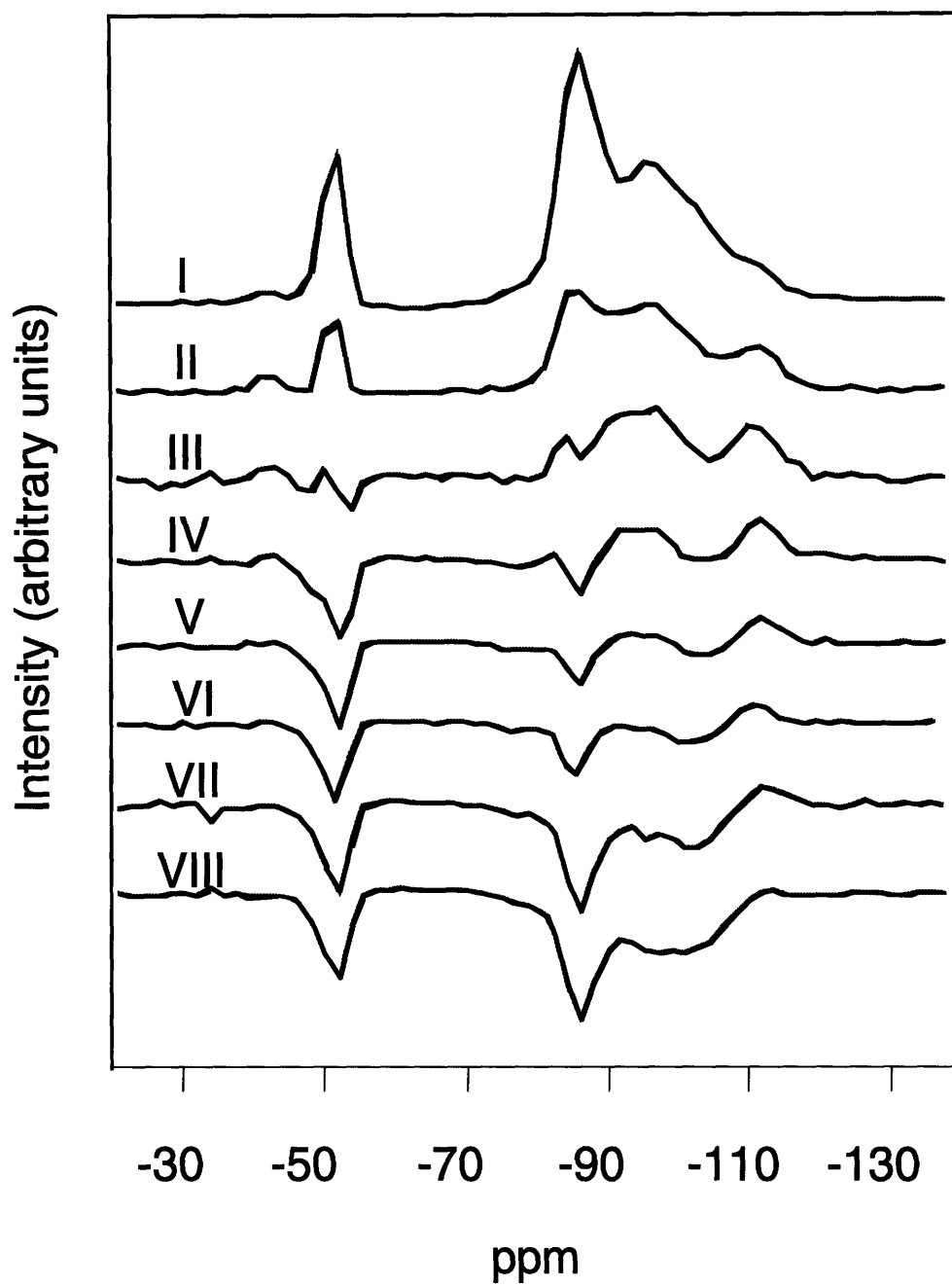


Figure 5.9 ^{29}Si NMR Polarization inversion spectra with different inversion time: i) 0.5 μs ; ii) 160 μs ; iii) 240 μs ; iv) 300 μs ; v) 360 μs ; vi) 480 μs ; vii) 640 μs ; viii) 960 μs ;

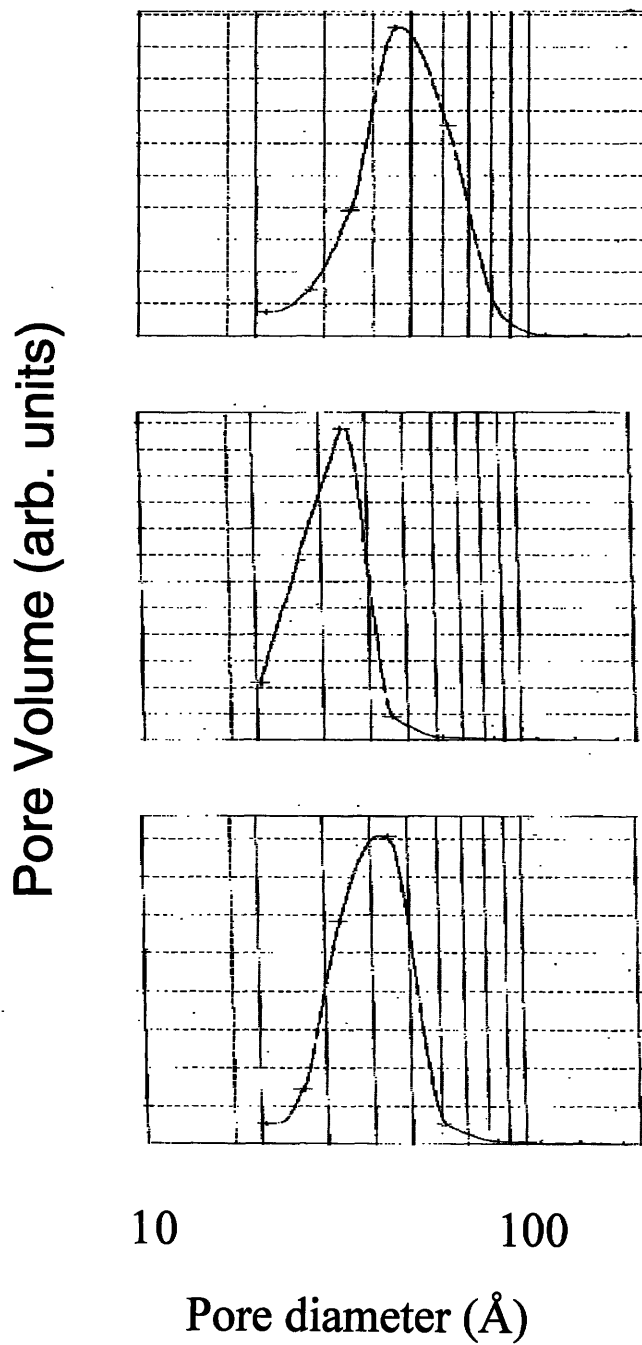


Figure 5.10 Pore size distribution: a) sample 1 (45 minutes); b) sample 2 (60 minutes); c) sample 3 (90 minutes);

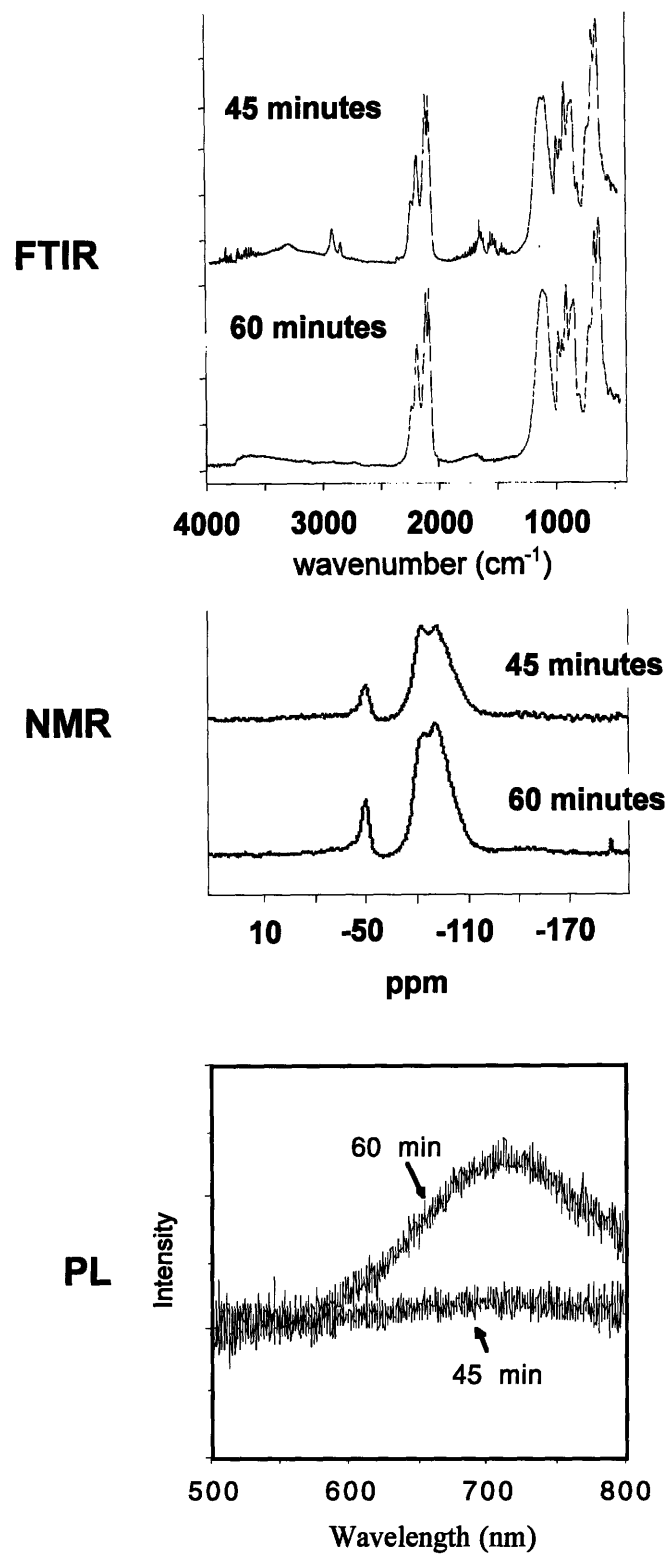


Figure 5.11 Comparison between the 45 and the 60 minutes samples: FTIR NMR and PL

Chapter 6. Conclusions

6.1 Summary

The objective of this thesis was to study the processing of porous silicon (PS) and to apply nuclear magnetic resonance (NMR) to study its surface chemistry. The main idea was to set up a series of porous silicon samples which were produced in an identical environment with the exception of only one processing parameter. As a result, we would be able to isolate the influence of that specific parameter on the properties of PS, especially its PL property and its surface chemistry. Because of the relative insensitivity of NMR (particularly for ^{29}Si , as it has a natural abundance of only 4.7 %) compared with other characterization methods, a large quantity of sample was required to acquire a relative clear signal within a reasonable measurement time. This brings an additional criterion for the processing of PS: while preserving the optical and mechanical properties, the PS sample had to be thick enough to provide a large enough quantity for characterization. For PS made from a 2" wafer, the minimum thickness was calculated to be $\sim 160 - 200 \mu\text{m}$. For a 4" wafer, the minimum thickness was $\sim 40 - 50 \mu\text{m}$. This requirement leads to another processing parameter: the anodization time. Although the dependence of the PS thickness and its density on the anodization time had been studied before, thickness of more than $50 \mu\text{m}$ was studied previously. Furthermore, pore structure and surface chemistry were not clearly correlated with PL properties.

Before the final set of PS sample were processed, a series of experiments were performed to study the dependence of the macroscopic properties (PL and mechanical stability) of PS on the processing parameters (current density, doping levels of the Si, HF concentration, and anodization time). The results of these experiments were used as the guidelines for the choice of the final parameters. The resulting PS could be roughly classified into three types. The first type of PS had the strongest PL intensity among all which could still be observed even under normal indoor lighting. However, mechanically it was quite fragile. Cracks started to develop on the PS layer surface when it was dried in air due to capillary forces. The second type of PS remained firmly intact on the wafer. However, it showed no, or very weak PL, which was hardly observable even in a very dim environment. The third type of PS was intermediate. PL could be easily observable in a darkened room, although not under normal indoor lighting. At the same time, it still remained intact on top of the wafer without forming cracks.

The results showed that an increase in the anodization current density, anodization time, and the resistivity of the Si wafers would tend to produce the first type of PS, which could also be achieved by a decrease in the HF concentration. This was generally in agreement with the expected pore structure of the material, which had been predicted by previous work. An important parameter that characterized the mechanical stability of PS was the inter-pore distance, which would determine whether the remaining Si wires could withstand the tensile stress developed during the drying process of PS or not. Besides, the inter-pore distance could also be related to the PL intensity according to the quantum confinement effect, which said that the small Si crystal would alter the band gap of the bulk Si and increase its photoluminescence efficiency. Therefore, the smaller the crystal, the higher would be its PL intensity. However, there are other factors that could affect the PL intensity as well, like surface chemistry. The real origin of PL in PS remains uncertain.

Anodization time could decrease the inter-pore distance in two ways: branching of the pores (which had a minimum value governed by the width of the depletion layer around the pores), and pure chemical etching. The dependence of the pore structure on the anodization time was consistent with the BET results of the final set of samples, which were only different in the anodization time. BET results showed 1) the surface area first increases, then decreases with the anodization time; and 2) a reverse trend in the pore diameter. That could be explained by the assumption that branching first increased in the beginning of the process, and after a period of time, the remaining Si wires collapsed as the pores met each other or be totally etched away when the anodization time increased further.

^1H , ^{19}F , and ^{29}Si NMR were used to study PS surface chemistry. ^1H and ^{19}F NMR were applied on a different set of samples supplied by the Spire Corporation, MA. The samples were different only in the anodization current density. PL had been measured on the freshly made samples. ^{19}F showed that there was only a very small amount of fluorine on the PS surface, which was consistent with the previous work and the assumed chemical reaction mechanism. PL and ^1H NMR of the same samples showed that there was no direct correlation between the PL property and the hydrogen content on the PS surface, which was found to decrease with the anodization current density. ^1H NMR of the old PS showed that hydrogen had been absorbed on the surface during the storage time in air, partially in the form of water molecules. Also, ^1H NMR showed that the pore surface of PS stored in air was not solely covered by $\text{Si}_2\text{-Si-H}_2$, as expected on a perfect (100) surface. Since the chemical shift range of the proton was too small to allow any resolution of the spectra, little chemical information

could be obtained. However, the abundance of protons on the surface would favor the detection of the less sensitive nuclei, ^{29}Si , which had a much larger chemical shift range.

^{29}Si NMR was employed on the final set of samples. As mentioned before, the only difference among them was the anodization time. The amount of HF consumed during the process in the electrolyte had been calculated. It was found that only a very small portion of HF was used up. Therefore the HF concentration could be considered to be roughly constant. It eliminated one potential cause for the change of the surface chemistry on PS over time. Also, the Thiele modulus was calculated for the experiments. The result showed that the concentration gradient of HF was negligibly small along the pores in PS. This eliminated another potential cause for the change of the PS surface chemistry. ^{29}Si was measured by the cross polarization - magic angle spinning (CPMAS) method. Cross polarization utilized the abundance of protons on the pore surface to enhance the ^{29}Si NMR signal. This would implicitly differentiate the chemistry of Si on the surface from that in the bulk. On the other hand, magic angle spinning suppressed the dipole-dipole interaction and the anisotropic chemical shift in the NMR signal, and resulted in a narrower NMR spectrum, which was necessary to resolve the overlapping peaks. To further assist the identification of the peaks in the spectra, inverse polarization technique was used, which was based on the dependence of the cross-polarization rate on the proton - silicon inter-nuclear distance.

As it was the first time PS was studied by ^{29}Si NMR, the assignments of the NMR signal were not totally certain. Therefore, ^{29}Si NMR spectra of the intentionally oxidized and reduced PS were measured for comparison. Corresponding samples were also examined by FTIR for further chemical information. The results confirmed that the samples in the final set were partially oxidized. Although not all NMR peaks were identified with certainty after these efforts, it laid the groundwork for further investigations of PS by this method.

Morphology measurements by BET and BJH of the final set of samples showed that the pore diameter distributions were monodisperse with the average pore diameters in the range of 30 to 60 Å. Combining with the estimation of the porosity in the samples, it was calculated that the wall thickness between the wires were in the range of 10 to 30 Å, which were small enough to induce quantum confinement effects.

6.2 Suggested Future Work

For the processing of PS, more work can be done. First, in order to look for further confirmation for the assumption that the inter-pore distances decrease with the depth of the PS layer, both plain view and cross-section TEM can be used to study the samples, which would provide a visual idea of the pore structure in the PS layer. The depth of the PS (after anodization) in the TEM sample could be adjusted by ion milling. Also, in order to process high porosity PS without damaging the Si wires, PS can be dried critically with CO₂, as it has been done previously [40].

In this thesis, only PS made from p-type Si was studied. It would be valuable to examine the difference of PS made from n-type Si as well. To produce n-type PS, an external illumination source will be needed to produce extra holes at the PS-electrolyte interface that are required in the initial step of anodization.

For the characterization of the sample, inverse polarization can be employed for the HF treated PS to further resolve the block around -100 ppm in the ²⁹Si spectra. Also, a more controlled oxidation (both in terms of the chemical environments and the temperature profile) of PS can be performed to assist the identification of the oxygen related peaks in the ²⁹Si spectra.

Bibliography

1. A. Uhler, *Bell Syst. Tech. J.*, **35**, 333 (1956).
2. R. L. Smith, and S. D. Collins, *J. Appl. Phys.*, **71** (8), R1-R22 (1992).
3. P. Steiner, and W. Lang, *Thin Solid Films*, **255**, 52-58 (1995).
4. L. T. Canham, *Appl. Phys. Lett.*, **57** (10), 1016-1048 (1990).
5. F. Namavar, H. P. Maruska, and N. M. Kalkhoran, *Appl. Phys. Lett.*, **60** (20), 2514-2516 (1992).
6. G. Bomchil, A. Halimaoui, I. Sagnes, P. A. Badoz, I. Berbezier, P. Perret, B. Lambert, G. Vincent, L. Garchery, and J. L. Regolini, *Appl. Surface Sci.*, **65/66**, 394-407 (1993).
7. T. Ito, and A. Hiraki, *J. Lumin.*, **57**, 331-339 (1993).
8. V. Grivickas, J. Linnros, and J. A. Tellefsen, *Thin Solid Films*, **255**, 208-211 (1995).
9. M. Niwano, J.-I. Kageyama, K. Kurita, K. Kinashi, I. Takahashi, and N. Miyamoto, *J. Appl. Phys.*, **76** (4), 2157-2163 (1994).
10. N. Ookubo, H. Ono, Y. Ochiai, Y. Mochizuki, and S. Matsui, *Appl. Phys. Lett.*, **61** (8), 940-942 (1992).
11. M. Jeske, J. W. Schultze, M. Thönissen, and H. Münder, *Thin Solid Films*, **255**, 63-66 (1995).
12. A. J. Steckl, J. Xu, H. C. Mogul, and S. M. Prokes, *J. Electrochem. Soc.*, **142** (5), L69-L71 (1995).
13. D. Rüter, and W. Bauhofer, *J. Lumin.*, **57**, 19-23 (1993).
14. W. Cao, and A. J. Hunt, *Appl. Phys. Lett.*, **64** (18), 2376-2378 (1994).
15. A. K. Vijh, *Electrochemistry of metals and semiconductors* (Marcel Dekker, New York, 1973).
16. S.-F. Chuang, PhD Thesis, Massachusetts Institute of Technology, 1990.
17. K. W. Cheah, and C. H. Choy, *Solid State Communications*, **91** (10), 795-797 (1994).
18. S. Frohnhoff, M. G. Berger, M. Thönissen, C. Dieker, L. Vescan, H. Münder, and H. Lüth, *Thin Solid Films*, **255**, 59-62 (1995).
19. D. I. Kovalev, and I. D. Yaroshetzki, *Appl. Phys. Lett.*, **64** (2), 214-216 (1994).
20. J. Wang, W.-C. Wang, J.-B. Zheng, F.-L. Zhang, X.-Y. Hou, X. Wang, H.-Z. Wang, and X.-G. Zheng, *Solid State Communications*, **91** (3), 239-243 (1994).
21. S. Schuppler; S. L. Friedman; M. A. Marcus; D. L. Adler; Y.-H. Xie; F. M. Ross; T. D. Harris; W. L. Brown; Y. L. Chabal; L. E. Brus, *et al.*, *Physical Review Letters*, **72** (16), 2648-2651 (1994).
22. M. Stutzmann, M. S. Brandt, E. Bustarret, H. D. Fuchs, M. Rosenbauer, A. Höpner, and J. Weber, *J. Non-Crystal. Solids*, **164-166**, 931-936 (1993).
23. A. G. Cullis, L. T. Canham, G. M. Williams, P. W. Smith, and O. D. Dosser, *J. Appl. Phys.*, **75** (1), 493-501 (1994).
24. P. M. Fauchet, E. Etedgui, A. Raisanen, L. J. Brillson, F. Seiferth, S. K. Kurinec, Y. Gao, C. Peng, and L. Tsybeskov, *Mat. Res. Soc. Symp. Proc.*, **298**, 271-275 (1993).
25. R. Czaputa, R. Fritzl, and A. Popitsch, *Thin Solid Films*, **255**, 212-215 (1995).
26. X. Wang, G. Shi, F. L. Chen, W. Wang, P. H. Hao, and X. Y. Hou, *Appl. Phys. Lett.*, **63** (17), 2363-2365 (1993).
27. A. Grosman, M. Chamarro, V. Morazzani, C. Ortega, S. Rigo, J. Siejka, and H. J. v. Bardeleben, *J. Lumin.*, **57**, 13-18 (1993).
28. R. Laiho, L. S. Vlasenko, M. M. Afanasiev, and M. P. Vlasenko, *J. Appl. Phys.*, **76** (7), 4290-4293 (1994).
29. Y. Xiao, T. J. McMahon, J. I. Pankove, and Y. S. Ysuo, *J. Appl. Phys.*, **76** (3), 1759-1763 (1994).

30. R. Sabet-Darmani, N. S. McAlpine, and D. Haneman, *J. Appl. Phys.*, **75** (12), 8008-8011 (1994).
31. S. Dannefaer, T. Bretagnon, A. Forcaran, T. Taliercio, and D. Kerr, *Thin Solid Films*, **255**, 171-173 (1995).
32. Y. Sasaki, and M. Mitahara, *J. Appl. Phys.*, **76** (7), 4344-4350 (1994).
33. A. Halimaoui, *Surface Science Letters*, **306**, L550-L554 (1994).
34. T. J. McMahon, and Y. Xiao, *Appl. Phys. Lett.*, **63** (12), 1657-1659 (1993).
35. C. L. Gupta, *J. Appl. Phys.*, **76** (8), 4800-4804 (1994).
36. M. Schoisswohl, H. J. v. Bardeleben, V. Morazzani, A. Grosman, and C. Ortega, *Thin Solid Films*, **255**, 123-127 (1995).
37. H. Unno, and S. Muramoto, *J. Electrochem. Soc.*, **134** (3), 645-648 (1987).
38. N. Ookubo, Y. Matsuda, Y. Ochiai, and N. Kuroda, *Mater. Sci. and Engineer.*, **B20**, 324-327 (1993).
39. U. Grüning, and A. Yelon, *Thin Solid Films*, **255**, 135-138 (1995).
40. S. Frohnhoff, R. Arens-Fischer, T. Heinrich, J. Fricke, M. Arntzen, and W. Theiss, *Thin Solid Films*, **255**, 115-118 (1995).
41. D. R. Turner, *The Electrochemistry of Semiconductors*; vol. 9, ed. by P. J. Holmes. Academic Press: London. 1962. pp 155-202.
42. D. H. Levy, and K. K. Gleason, *J. Vac. Sci. Technol. A*, **11** (1), 195-198 (1993).
43. A. Prutton, *Surface Physics* (Charendon, 1975).
44. D. H. Levy, and K.K.Gleason, *J. Electrochem. Soc.*, **140** (3), 797-800 (1993).
45. O. Levenspiel, *The Chemical Reactor Omnibook* (OSU Book Stores, Inc., Corvallis. 1993).
46. A. Borghesi, G. G. Guizzetti, A. Sassella, O. Bisi, and L. Pavesi, *Solid State Communications*, **89** (7), 615-618 (1994).
47. Z. C. Feng, A. T. S. Wee, and K. L. Tan, *Journal of Physics D: Applied Physics*, **27**, 1968-1975 (1994).
48. É. B. Vázsonyi, M. Koós, G. jalsovszky, and I. Pócsik, *Thin Solid Films*, **255**, 121-124 (1995).
49. P. O'Keefe, and Y. Aoyagi, *Appl. Phys. Lett.*, **66** (7), 836-838 (1995).
50. A. Borghesi, S. Sassella, B. Pivac, and L. Pavesi, *Solid State Communications*, **87** (1), 1-4 (1993).
51. Y. Ogata, H. Niki, T. Sakka, and M. Iwasaki, *J. Electrochem. Soc.*, **142** (1), 195-201 (1995).
52. P. Gupta, A. C. Dillon, A. S. Bracker, and S. M. George, *Surface Science*, **245**, 360-372 (1991).
53. Y. Kato, T. Ito, and A. Hiraki, *Appl. Surface Sci.*, **41/42**, 614-618 (1989).
54. G. Engelhardt, and H. Koller, *Solid-State NMR II, Inorganic Matter*; vol. 31, ed. by B. Blümich. Springer-Verlag: Berlin. 1994. pp 1-31.
55. C. R. Ernst, L. Spialter, G. R. Buell, and D. L. Wilhite, *J. Am. Chem. Soc.*, **96** (17), 5375-5380 (1974).
56. N. Janes, and E. Oldfield, *J. Am. Chem. Soc.*, **107** (24), 6769-6775 (1985).
57. X.-D. Cong, R. J. Kirkpatrick, and S. diamond, *Cement and Concrete Research*, **23**, 811-823 (1993).
58. W.-L. Shao, J. Shinar, and B. C. Gerstein, *Phys. Rev. B*, **41** (13), 9491-9494 (1990).
59. F. R. Jeffery, P. D. Murphy, and B. C. Gerstein, *Phys. Rev. B*, **23** (5), 2099-2101 (1981).
60. B. Lamotte, A. Rousseau, and A. Chenevas-Paule, *Recent Developments in Condensed Matter Physics*; vol. 2, ed. by J. T. Devreese, L. F. Lemmens, V. E. V. Doren, and J. V. Royen. Plenum Press: New York. 1981. pp 247-251.
61. N. Zumbulyadis, *J. Chem. Phys.*, **86** (3), 1162-1166 (1987).
62. J. M. Smith, *Chemical Engineering Kinetics*; 3rd ed. (McGraw-Hill, New York. 1981).
63. L. H. Cohan, *J. Am. Chem. Soc.*, **60**, 433 (1938).